Results of Intercomparisons of the OFM and the RFM Code PO-TN-OXF-GS-0007

Anu Dudhia* Piera Raspollini†

December 9, 1996

Abstract

This report describes the results of intercomparisons between the MIPAS Optimised Forward Model (OFM) and Reference Forward Model (RFM) codes. It is produced as a combination of Tasks 2.1 from the OFM/ORM study (PO-SW-ESA-GS-0315) and Task 3.3 from the RFM study (PO-SW-ESA-GS-00323).

The primary purpose of this intercomparison is to identify and rectify any problems in the OFM and/or RFM codes. A secondary purpose is to quantify the residual OFM-RFM differences prior to using RFM-generated spectra as simulated observations for testing the full MIPAS retrieval algorithm.

The intercomparison is organised as a sequence of progressively more complex tests, starting with tests of individual OFM sub-modules, proceeding through ray tracing and homogeneous path spectral calculations to spectral calculations for limb paths, and finishing with comparisons of apodised and field-of-view-convolved radiance spectra for six typical MIPAS microwindows (one for each target species).

The RFM v2 code is used as the fixed baseline and compared to the most up-to-date version of the OFM code. The effects of specific improvements to the RFM code are also discussed.

The results show that the microwindow calculations for stratospheric limb paths meet the requirement for agreement within ±NESR/4, but not the calculations for low altitudes. The disagreement at low altitude has been identified as due to problems with the FOV convolution in both the RFM and OFM, and also the non-LTE formulation of the RFM radiative transfer. The impact of these radiance differences on retrieval errors is also evaluated.

It is recommended that the OFM FOV-convolution be investigated further, and that some of the low-altitude reference spectra created by the RFM v2 be recalculated using the improvements identified here.

Acknowledgements: The authors would like to thank the following for their contributions to the work presented in this report: Bruno Carli, Massimo Carlotti, David Edwards, Jean-Marie Flaud, Michael Höpfner, Eugenio Lunedei, Paul Morris, Marco Ridolfi and Gabrielle Stiller.

*Atmospheric, Oceanic and Planetary Physics, Oxford University, UK
†Istituto di Ricerca sulle Onde Elettromagnetiche, Firenze, Italy

Contents

List of Tables

List of Figures

List of Abbreviations

ALS	Apodised Instrument Line Shape
ESA	European Space Agency
FFT	Fast Fourier Transform
FOV	Field of View
IMK	Institut für Meteorologie und Klimaforschung
IROE	Istituto di Ricerca sulle Onde Elettromagnetiche
ISAMS	Improved Stratospheric and Mesospheric Sounder
LTE	Local Thermodynamic Equilibrium
MIPAS	Michelson Interferometer for Passive Atmospheric Sounding
MW	Microwindow
NESR	Noise Equivalent Signal Radiance
NRT	Near Real Time
OFM	Optimised Forward Model
ORM	Optimised Retrieval Model
ppmv	Parts per million by volume
RFM	Reference Forward Model
SOW	Statement of Work
TIPS	Total Internal Partition Sum
US76	US 1976 Standard (Atmosphere)
vmr	Volume mixing ratio

Applicable Documents

ESA

PO-SW-ESA-GS-00315 Development of an optimised algorithm for routine p,T and VMR retrievals from MIPAS limb emission spectra.

PO-SW-ESA-GS-00323 Development of a Reference Forward Algorithm for the Simulation of MIPAS Atmospheric Limb Emission Spectra.

RFM

PO-RS-OXF-GS-0002 Software Requirements Document

PO-MA-OXF-GS-0003 Software User's Manual

PO-TN-OXF-GS-0004 High-Level Algorithms Definition

PO-TN-OXF-GS-0006 Results of Intercomparisons with the RFM Code and External Reference Models

OFM

TN-IROE-RSA9601 High level algorithm definition and physical and mathematical optimisations.

Introduction

Background

The Michelson Interferometer for Passive Atmospheric Sounding (MIPAS) is an ESA-developed instrument to be flown on the ENVISAT-1 satellite as part of the first Polar Orbit Earth Observation Mission program (POEM-1). MIPAS will perform limb sounding observations of the atmospheric emission spectrum in the middle infrared region and derive profiles of pressure, temperature and concentration of various species.

The envisaged operational scheme is to retrieve p, T profiles, followed by O_3, H_2O, HNO_3, CH_4 and N_2O, all in near real time (NRT). The retrieval of these parameters from calibrated spectra (Level 1b data) is termed 'NRT Level 2 processing'.

Level 2 processing is expected to be a critical part of the Payload Data Segment (PDS) because of both the long computing time that may be required and the need for a validated algorithm capable of producing accurate and reliable results.

As with most satellite retrieval schemes, the scientific code developed as the basis for Level 2 processing software can be thought of as having two components: the Optimised Forward Model (OFM), used to calculate the observations (radiance spectra in this case) expected from a given atmospheric state (i.e. profiles of p, T, and vmrs); and the Optimised Retrieval Model (ORM), used to determine the atmospheric state given a set of observations [1]. Broadly speaking, the OFM is the radiative transfer calculation within the ORM, which is itself a purely statistical operation. The 'optimisation' refers to the requirement that the retrieval be performed in NRT hence it represents a compromise between speed and accuracy. The OFM/ORM code will be used for the development of the industrial prototype for the operational Level 2 code. For convenience a stand-alone version of the OFM code has also been developed, and this is the actual model tested here.

The MIPAS Reference Forward Model (RFM) is a line-by-line model, derived from GENLN2 [2], which has been developed as a general-purpose spectral model for use by the MIPAS community [3]. Apart from the flexibility required from such a model, the RFM is also intended to perform calculations with the emphasis on accuracy rather than computation speed, and so generate spectra which can be regarded as 'truth' for testing the OFM/ORM. The RFM v2 code ('Version 2') is the version currently distributed by ESA and is used as a baseline for the intercomparisons, although the effects of modifications to this code are also considered.

Scope of this Report

The purpose is to evaluate and explain the differences between the RFM and OFM algorithms and to suggest where improvements are required. These results also have a bearing on the OFM/ORM retrieval tests using reference spectra generated by the RFM.

For this intercomparison four groups of tests were devised, representing progressively more complex calculations.

1. Critical Sub-Modules

   Test 1.1 Calculation of Gravity

   Test 1.2 Integration of Hydrostatic Equation

   Test 1.3 Calculation of Refractivity

   Test 1.4 Apodised Line Shape

2. Ray-Tracing

   Test 2.1 Path Length

   Test 2.2 Path Column Amount

   Test 2.3 Curtis-Godson Parameters

3. Spectral Calculations for Homogeneous Paths

   Test 3.1 Voigt Line Shape

   Test 3.2 ALS Convolution

   Test 3.3 Line Wings

   Test 3.4 Microwindow Absorption

4. Spectral Calculations for Limb Paths

   Test 4.1 Limb Absorption

   Test 4.2 Limb Radiance Convolutions

   Test 4.3 Microwindow Radiances

Each of these tests forms a separate section of this document.

Acceptance Criteria

Before comparisons were started, criteria were established to define the 'acceptable' limits of discrepancies. These are based on the assumption that the forward model errors should not significantly detract from the estimated performance of MIPAS and the theoretical accuracy of the retrieved parameters, which in practice means setting a limit of 25% of these values. According to the quantities being compared, these criteria are:

- $\pm$NESR/4 in apodised radiance spectra
- $\pm$0.75% in pressure (equivalent to $\pm$50 m in altitude)
- $\pm$0.5 K in temperature
- $\pm$1.25% in vmr

Table 1: Difference between acceleration due to gravity evaluated by the OFM/ORM algorithm (g_O) and the ISAMS algorithm (g_I), as a function of latitude and altitude. Values are % difference: $100(g_O - g_I)/g_I$. In brackets are the % variations $100(g_I - g_0)/g_I$ from the standard value g_0=9.80665 m s^{-2}.

Altitude [km]	% Diff at Equator	% Diff at 45°	% Diff at Pole
0	−0.0007 (−0.27)	−0.0026 (−0.00)	+0.0006 (+0.26)
50	+0.0019 (−1.82)	−0.0038 (−1.56)	−0.0046 (−1.30)
100	+0.0044 (−3.34)	−0.0051 (−3.08)	−0.0095 (−2.81)

Databases & Assumptions

The following databases and assumptions are used for the calculations:

Atmosphere FASCODE 'MODEL 6' Atmosphere (1976 US Standard) augmented with the HNO_3 profile from the 'MINGAS' section. Used with original layering, i.e. 1 km layers up to 25 km, 2.5 km layers up to 50 km, and 5 km layers up to 100 km (OFM) or 120 km (RFM). Local radius of curvature assumed to be 6367.421 km.

Line Data HITRAN '96, although the RFM v2 uses the '92 TIPS data and both the RFM and OFM use the '92 TIPS HNO_3 data (section 6.1).

Line Shape The Norton-Beer no.3 (Strong) Apodisation [4] is used in spectral space, assuming a maximum path difference of 20 cm. No extra instrumental effects are considered (section 1.4).

Field-of-View A trapezoidal response is assumed: constant out to ±1.4 km from the nominal tangent point, then reducing linearly to zero at ±2.0 km. No allowance is made for distortion due to refraction.

Interpolation For these comparisons both the RFM and OFM interpolate $\ln p$, T and vmr linearly between profile levels.

1 Critical Submodules

This sections tests critical sub-modules of the OFM which are either not used within the RFM, or for which the RFM intentionally uses the OFM algorithms (e.g. refractivity). For this reason, external references are required which are either derived from the ISAMS software [5] or GENLN2 [2].

1.1 Gravity

The acceleration due to gravity g is required within the OFM/ORM for the integration of the hydrostatic equation in the p, T retrieval. The algorithm used is based on an empirical function of latitude to which the altitude dependence is then added [6].

The RFM does not employ any hydrostatic balance, hence has no calculation of g. In this case, the external reference is the algorithm used within p, T retrievals from the ISAMS instrument. The ISAMS algorithm is based on a Legendre polynomial expansion of the gravitational potential [7] to degree 2, coupled with an ellipsoidal model of the earth shape, to which a rotational acceleration is added.

The results of the comparison are shown in Table 1.

An assessment of the impact of the difference can be obtained by considering an integration of the hydrostatic equation assuming constant temperature T:

$$\Delta \ln p = -\left(\frac{gM}{RT}\right)\Delta z \tag{1}$$

Table 2: Difference between pressure calculated by the OFM (p_O) and ISAMS (p_I) hydrostatic integration algorithms using $T(z_i)$ from US76 Atmosphere. Also, for comparison, are the differences between ISAMS pressures and the US76 Atmosphere pressures p_U.

Altitude [km]	p_O [mb]	p_I [mb]	% Difference $100(p_O - p_I)/p_I$	p_U [mb]	% Difference $100(p_U - p_I)/p_I$
10	265.473	265.467	+0.002	265.0	−0.176
20	55.9350	55.9321	+0.005	55.29	−1.161
30	12.1144	12.1134	+0.009	11.97	−1.198
40	2.91710	2.91675	+0.012	2.871	−1.593
50	0.807569	0.807443	+0.016	0.7978	−1.209
60	0.221629	0.221586	+0.019	0.2190	−1.181
70	0.0527190	0.0527063	+0.024	0.05220	−0.970
80	0.01064845	0.01064528	+0.030	0.01050	−1.384
90	0.00186212	0.00186144	+0.036	0.001840	−1.165
100	0.00032410	0.00032396	+0.043	0.0003200	−1.236

From this it can be seen that errors in g translate proportionally into errors in the integrated differences in $\ln p$ or z. Assuming an average error in g of 0.005% (from the 'Pole' column in Table 1), this will contribute an error of 2.5 m in z when integrating over 50 km (equivalent to a pressure error of 0.0035% assuming a pressure change of 1% per 70 m).

It is concluded that differences in algorithms to evaluate g are negligible.

1.2 Hydrostatic Integration

The assumption of hydrostatic balance is a useful constraint on a simultaneous p, T retrieval from a limb-sounder since it removes the requirement that pressure and temperature be retrieved independently at each altitude. As mentioned in the previous section, hydrostatic balance is not required for the RFM so the OFM/ORM algorithm has been compared with an equivalent module from the ISAMS p, T retrieval.

The hydrostatic equation can be expressed as:

$$\int \frac{dp}{p} = -\int \left(\frac{gM}{RT}\right) dz \tag{2}$$

There are several methods for numerically integrating Eq. 2 depending on the assumptions made about the terms in the brackets on the right hand side. The form of $g(z)$ has been discussed in the previous section, values of M (usually) and R are constant, but the value of T can be assumed to be either an average value $\langle T \rangle$ between levels, or an average value of $\langle 1/T \rangle$, or a linear function of z. ISAMS and OFM/ORM both employ the same algorithm: assuming average layer values of $\langle T \rangle$ and $\langle g \rangle$ within each step.

The two algorithms have been compared using the set of US76 temperatures and altitudes $T(z_i)$ as a basis, starting at the surface pressure (1013.0 mb in this case, i.e. not 1013.25 mb). The US76 nominal latitude of 45.5397° was assumed for calculating g using the individual ISAMS and OFM algorithms in the previous section. The results at 10 km intervals are are shown in Table 2. Also shown for comparison are the differences between the ISAMS calculation and the US76 pressures, although these are influenced by the lack of precision (3–4 sig.figs) of the US76 data.

The maximum discrepancy of around 0.05% in pressure (equivalent to 3.5 m in altitude) is not significant for the p, T retrieval.

1.3 Refractivity

The refractive index of air varies as a function of density and wavelength, and also with water vapour content.

A convenient method for expressing refractive index n is in terms of the refractivity N, defined as:

$$N = (n - 1) \times 10^6 \tag{3}$$

Table 3: Difference between refractivity N ($= (n-1) \times 10^6$) calculated from corrected GENLN2 algorithm (N_G, includes ν and H_2O dependence) and OFM algorithm (N_O), assuming US76 Atmosphere.

Altitude [km]	N_G@ 600 cm^{-1}	N_G@ 2500 cm^{-1}	N_O	δz [m] @ 600 cm^{-1}	δz [m] @ 2500 cm^{-1}
0	270.747	270.836	272.527	−11.4	−10.8
5	163.692	163.746	163.892	−1.3	−0.9
10	92.006	92.036	92.013	−0.1	+0.1
15	43.327	43.342	43.329	−0.0	+0.1
20	19.782	19.789	19.783	−0.0	+0.0
25	8.918	8.921	8.919	−0.0	+0.0
30	4.097	4.099	4.098	−0.0	+0.0

The OFM algorithm uses a simplified version of the Edlén formula ([8]) reduced to a function of air density by neglecting the water vapour contribution and evaluating the coefficients at a fixed wavelength 8.94 μm.

The GENLN2 algorithm was chosen for comparison[1]. GENLN2 is required to calculate refractivity over a wider range of wavenumbers and water vapour partial pressures than the OFM, so uses the full Edlén's formula (e.g. as cited in [9]). However, the GENLN2 v.3 code does appear to use the incorrect reference temperature (0°C) for the density dependence, so in these calculations it has been altered to use the correct value 15°C.

Values of the OFM refractivity at various altitudes (i.e. densities within the US76 Atm.) have been evaluated and compared with the (corrected) GENLN2 algorithm at the two extremes of the MIPAS spectral range (600 cm^{-1} and 2500 cm^{-1}), assuming the US76 water vapour profile. This tests both the assumptions and implementation of the OFM algorithm. The results are shown in Table 3.

The OFM values of refractivity are generally higher than the GENLN2 values in the troposphere, which is consistent with the OFM assumption of dry air (moist air has a lower refractive index [9]), and lie between the GENLN2 values in the stratosphere, as expected given the 8.94 μm (~1120 cm^{-1}) nominal wavelength.

To assess the impact of these differences, consider the standard expression for ray tracing in a spherical, refracting atmosphere:

$$nr = \text{constant} \tag{4}$$

where r is the distance from the centre of curvature. This can be expanded to relate a refractivity error δN to an altitude error δz at the tangent point:

$$(1 + (N + \delta N) \times 10^6)(R_\oplus + z + \delta z) = \text{constant} \tag{5}$$

where $R_\oplus$ is the radius of the earth (approx. 6400 km), hence δz [m] $\simeq -6.4 \times \delta N$.

The lowest altitude likely to be required for MIPAS calculations (allowing for the FOV convolution) is 5 km, so the maximum error arising from the OFM assumptions on refractivity are of the order of 1 m, i.e. negligible.

1.4 Apodisation

The MIPAS spectra will have an apodisation function applied to the interferograms corresponding to the Norton-Beer no.3 (Strong) apodisation function [4]. The OFM simulates this by applying a convolution function in spectral space to represent the combined effects of this apodisation and the instrumental self-apodisation. The combined function is known as the Apodised Instrument Line Shape (ALS), but since the instrumental component was not known at the start of these tests, a sinc function with 0.025 cm^{-1} resolution (=1/(2× max.path difference)) was assumed, so that the ALS is simply the apodisation function. This ALS, labelled the 'IROE' function in this study, is represented at 0.0005 cm^{-1} resolution, truncated at ±0.175 cm^{-1}, giving a total of 701 points.

[1] The RFM uses either the OFM or the GENLN2 algorithms

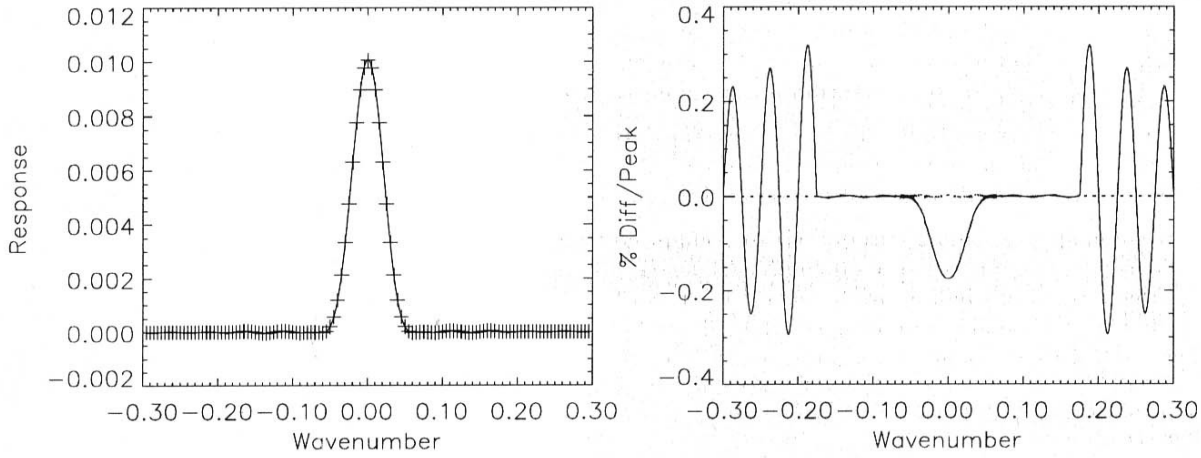

Figure 1: Comparison of GENLN2 FFT calculation (solid line) of the Norton-Beer Strong Apodisation function with the IROE explicit evaluation (crosses). The right plot shows the IROE-FFT differences (solid line), together with the difference if the FFT function is truncated and renormalised within the ± 0.175 cm^{-1} range (dotted line) to match the IROE function.

To provide an independent test of the IROE function, the GENLN2 FFT routine was used to derive the spectral function from the Norton-Beer apodisations in interferogram space (this is similar to the procedure that will be used to apodise the actual measured spectra, as opposed to the forward model calculations). The spectral function was also generated at 0.0005 cm^{-1} resolution, but extended to ± 0.3 cm^{-1} (=1201 points) to test the effects of the OFM truncation. This ALS will be labelled the 'FFT' function in this study. The results are shown in Fig. 1.

When both functions are truncated at ± 0.175 cm^{-1} the agreement (dotted line) is to better than 0.01% of the peak value. However, when compared with the extended function (± 0.3 cm^{-1}) the major source of disagreement (0.3%) can be seen to be caused by the truncation rather than the detailed shape. The extended function also differs by around 0.15% in the peak but this is simply due to the renormalisation allowing for the extra half-oscillation beyond ± 0.275 cm^{-1}.

The operational details of the MIPAS interferogram apodisation are not yet known (e.g. the FFT ALS is sensitive to the number of points used: 2^{20} in this case) so the FFT ALS should not be regarded as definitive. For this reason, most RFM calculations in this study were performed with the same IROE ALS function as the OFM calculations, and the verification of the IROE ALS is left as an open issue. However, the impact of the IROE-FFT ALS difference is discussed further in sections 3.2 and 4.1.

2 Path Calculations

This section tests the ray-tracing algorithms of the OFM and the RFM, together with the integration of various quantities along the ray path.

The two models use quite different ray-tracing techniques. The OFM uses distance-from-tangent-point as the integration variable [6] while the RFM uses altitude (the RFM algorithm follows closely that of GENLN2, which is itself derived from FASCODE [10]).

For these and subsequent tests a local radius of curvature of 6367.421 km has been assumed.

Table 4: Difference between path lengths calculated by OFM s_O and RFM s_R through US76 Atmosphere for different tangent heights. The % difference is $100(s_O - s_R)/s_R$.

	Without Refraction				With Refraction			
Tan.Hgt [km]	s_O [km]	s_R [km]	Diff. [km]	Diff. [%]	s_O [km]	s_R [km]	Diff. [km]	Diff. [%]
60	880.281	880.279	+0.002	+0.0002	880.293	880.291	+0.002	+0.0002
40	1015.692	1015.671	+0.021	+0.0021	1015.866	1015.850	+0.016	+0.0016
10	1189.689	1189.594	+0.095	+0.0080	1209.057	1208.975	+0.082	+0.0068

Table 5: Difference between refracted path total gas amounts U_O (OFM) and U_R (RFM) for CO_2 and N_2O and for different tangent paths through the US76 Atmosphere. The % difference is $100(U_O - U_R)/U_R$.

	CO_2			N_2O		
Tan.Hgt [km]	U_O [kmole/cm^2]	U_R [kmole/cm^2]	Diff. [%]	U_O [kmole/cm^2]	U_R [kmole/cm^2]	Diff. [%]
60	9.67719×10^{-8}	9.67900×10^{-8}	−0.019	5.08672×10^{-13}	5.08778×10^{-13}	−0.021
40	1.23689×10^{-6}	1.23689×10^{-6}	−0.000	1.08289×10^{-9}	1.08290×10^{-9}	−0.001
10	1.26046×10^{-4}	1.26011×10^{-4}	+0.028	1.13409×10^{-7}	1.13375×10^{-7}	+0.030

2.1 Path Length

The simplest test is a comparison of integrated path length through the atmosphere (defined by an upper boundary at 120 km), both with and without refraction effects. The results are shown in Table 4, for three different tangent heights.

These show significantly increased differences at the lower altitudes, but these differences are not especially sensitive to the refraction. This suggests that the low altitude discrepancies are larger just as a result the accumulated differences between the two numerical integration schemes as more sub-paths are considered.

The largest difference (at 10 km) corresponds to an error of $< 0.001\%$ in path length. This would be expected to contribute a similar (i.e. negligible) error in column amount and retrieved vmr.

2.2 Column Amount

The primary path integral is the total absorber amount U_g (kmoles/cm^2) obtained by integrating the molar absorber density ρ_g (kmoles/cm^3) along the ray path s.

$$U_g = \int_{\text{path}} \rho_g \, ds \tag{6}$$

Since ρ_g is the product of the volume mixing ratio and the (molar) air density, for a gas with constant vmr profile (e.g. CO_2) this is equivalent to an integration of the air density. For other gases there is an additional vertical gradient superimposed: N_2O was also chosen for comparison since it has a steep vertical gradient throughout the stratosphere. The results are shown in Table 5.

The % differences are somewhat larger than just due to path length (Table 4), and of alternating sign, suggesting that the numerical integration of Eq. 6 introduces a further discrepancy. The % differences for the two gases are similar at each height, so the error appears to be independent of the shape of the vmr profile.

The maximum difference is ~0.03%, which is expected to translate into the same error in retrieved vmr, and is still negligible.

Table 6: Comparison of Curtis-Godson equivalent pressure and temperature for various segments (defined by altitude boundaries) of a 10 km tangent-height path for N_2O assuming US76 Atmosphere. For information, the OFM-RFM % difference in segment absorber amount u_g is also shown (column 2).

Segment	Abs.Amt.	Curtis-Godson Pressure			Curtis-Godson Temperature		
Low–High [km]	Diff. u_g [%]	$\bar{p}_{gO}$ [mb]	$\bar{p}_{gR}$ [mb]	Diff. [%]	$\bar{T}_{gO}$ [K]	$\bar{T}_{gR}$ [K]	Diff. [K]
90–95	−0.0009	.00131886	.00131884	+0.0015	187.5151	187.5151	0.0000
47.5–50	−0.0005	0.9602974	0.9602863	+0.0012	270.6418	270.6418	0.0000
10–11	+0.0671	252.41988	252.41111	+0.0035	221.2145	221.2130	+0.0015

2.3 Curtis-Godson Parameters

Both the OFM and the RFM use the Curtis-Godson approximation for limb-path calculations. This assumes that the (inhomogeneous) limb path can be divided into segments, each segment having a transmission equivalent to a homogeneous path containing the same absorber amount u_g and the 'Curtis-Godson' equivalent pressure $\bar{p}_g$ and temperature $\bar{T}_g$ defined by:

$$u_g = \int_{\text{seg}} \rho_g \, ds \tag{7}$$

$$\bar{p}_g = \frac{1}{u_g} \int_{\text{seg}} p \rho_g \, ds \tag{8}$$

$$\bar{T}_g = \frac{1}{u_g} \int_{\text{seg}} T \rho_g \, ds \tag{9}$$

Discrepancies in $\bar{p}_g$ or $\bar{T}_g$ may arise either from the computation of the weighted integrals (Eqs. 8–9), or from the computation of the segment absorber mass, u_g (Eq. 7).

For the intercomparison, the Curtis-Godson equivalent parameters were compared for N_2O for various segments of a 10 km tangent path, the species and tangent height being the 'worst-case' agreement from the previous section. The results are shown in Table 6. Also shown are the differences between the OFM and RFM calculations of absorber amount u_g for each segment.

The results show differences in pressure of less than 0.004% and temperature of less than 0.002 K. It is notable that the pressure and temperature discrepancies for the lowest path segment (10–11 km) are significantly less than the difference in the absorber amount for that segment, implying that while the OFM-RFM integration methods for Eqs 6–9 are different, they are at least self-consistent. This is also generally true of other levels not shown in the table: the Curtis-Godson pressure and temperature discrepancies remain roughly the same, while the absorber amount discrepancies for the 47.5–50 km and 90–95 km segments are anomalously low and values of 0.01% are more typical.

The differences in the Curtis-Godson parameters $\bar{p}_g, \bar{T}_g$ are well within the precision that will be obtainable from the MIPAS p, T retrieval (3%, 2 K), so can be regarded as negligible.

3 Spectral Calculations

This sequence of tests compares the RFM and OFM spectral calculations using fully-defined homogeneous paths (i.e. without any ray-tracing). Two different wavenumber grids are used:

Fine Grid 0.0005cm^{-1} spacing (2000 pts/wavenumber)

Coarse Grid 0.025cm^{-1} spacing (40 pts/wavenumber)

The Fine Grid is that commonly used for middle-atmosphere line modelling (Doppler-broadened half-widths of atmospheric lines are typically >0.001 cm^{-1}) and is used by both models for internal calculations. The Coarse Grid is the MIPAS standard for representing apodised spectra.

3.1 Voigt Line Shape

Atmospheric lines are generally well-described by the Voigt line shape, which represents a convolution of the Lorentz (pressure-broadened) and Doppler (velocity-broadened) line shapes. The standard numerical algorithm for computing the Voigt line shape, due to Humlicek [11], is implemented by both the OFM and RFM with various modifications for efficiency, especially in the line wings. To test these algorithms the CO_2 line at 952.880858 cm^{-1} is isolated and calculations performed for three different regimes:

(a) Lorentz: p=250 mb, T=220 K (typical atmospheric conditions at 10 km altitude)

(b) Mixed: p=2.5 mb, T=250 K (~40 km altitude)

(c) Doppler: p=0.2 mb, T=240 K (~60 km altitude).

In all cases the CO_2 vmr was set to 330 ppmv (US76 value) and the pathlength to 250 km (approximately the length of a limb path within 5 km altitude of the tangent point). The results are shown in Fig. 2.

The diagnostic plotted is optical depth, χ, a dimensionless variable proportional to the absorption coefficient k:

$$\chi(\nu) = \int_{\text{path}} k(\nu)\rho_g \, ds \tag{10}$$

For a homogeneous path the integral is trivial. To illustrate the comparisons in the line wings, a logarithmic scale is used for the optical depth axis, and the % difference at each point is also plotted.

The 'oscillations' in the Lorentzian case (a) arise from the OFM's use of a variable grid spacing: to save time, the line-shape for broad lines is only calculated explicitly on a subset of the fine grid points and intermediate points are obtained by linear interpolation. The discontinuities arise from transitions in the OFM grid-spacing, and from the transition from Voigt to Lorentz line-shape in the line wings. The accuracy associated with the OFM line-shape interpolation appears to be of the order of 0.15% at the peak.

For the narrow lines in (b) and (c), the OFM calculates line shape explicitly at each fine grid point, so no oscillations are present, but there are unexplained peaks (actually 'dips' in terms of the magnitude of the difference) at around ± 0.005 cm^{-1} from the line centre. Both difference plots appear to level out at -0.05% difference suggesting a constant scaling factor discrepancy in absorption coefficient.

The calculated line strength includes scaling by a temperature dependent 'Total Internal Partition Sum' (TIPS) factor (described in section 5.3). The RFM v2 uses the '92 TIPS data whereas the OFM uses the '96 version, and recalculating the RFM optical depth with the '96 TIPS shows that this accounts for most of the offset in the % difference plot.

After correcting for the different TIPS data, all three differences tend to a residual difference of -0.0125% in the line wings, possibly due to a difference in precision of one or more of the constants used in the line shape algorithms, or to the addition/subtraction of offsets as part of the OFM variable gridding. In regions of low total absorption $a \simeq \chi \ll 1$, so this will contribute the same proportional difference in absorption and radiance (i.e. negligible), and less in regions of high absorption due to the non-linear relationship between a and χ. In terms of absolute absorption, this offset is negligible.

It is concluded that the OFM Voigt line-shape approximations contribute an oscillatory error of up to 0.2%, and the OFM-RFM line shapes have a systematic difference of 0.01% when using the same TIPS data.

3.2 ALS Convolution

To test the application of the apodisation function and its influence on the discrepancies noted in the previous section, the absorption spectra a $(= 1 - \exp(-\chi))$ for the same three homogeneous path conditions were convolved with the apodisation functions $\Psi(\nu' - \nu)$ described in section 1.4.

$$a_{\text{als}}(\nu) = \int \Psi(\nu' - \nu) a(\nu') \, d\nu' \tag{11}$$

where the limits of integration are ± 0.175 cm^{-1} for the IROE function, and ± 0.3 cm^{-1} for the FFT-derived function. Because of the significant offsets caused by the use of the '92 TIPS data, the RFM calculations for this particular case were performed with the '96 TIPS to isolate the effects of the ALS convolution. The RFM results were calculated for two cases: using either the IROE or the FFT ALS function (section 1.4).

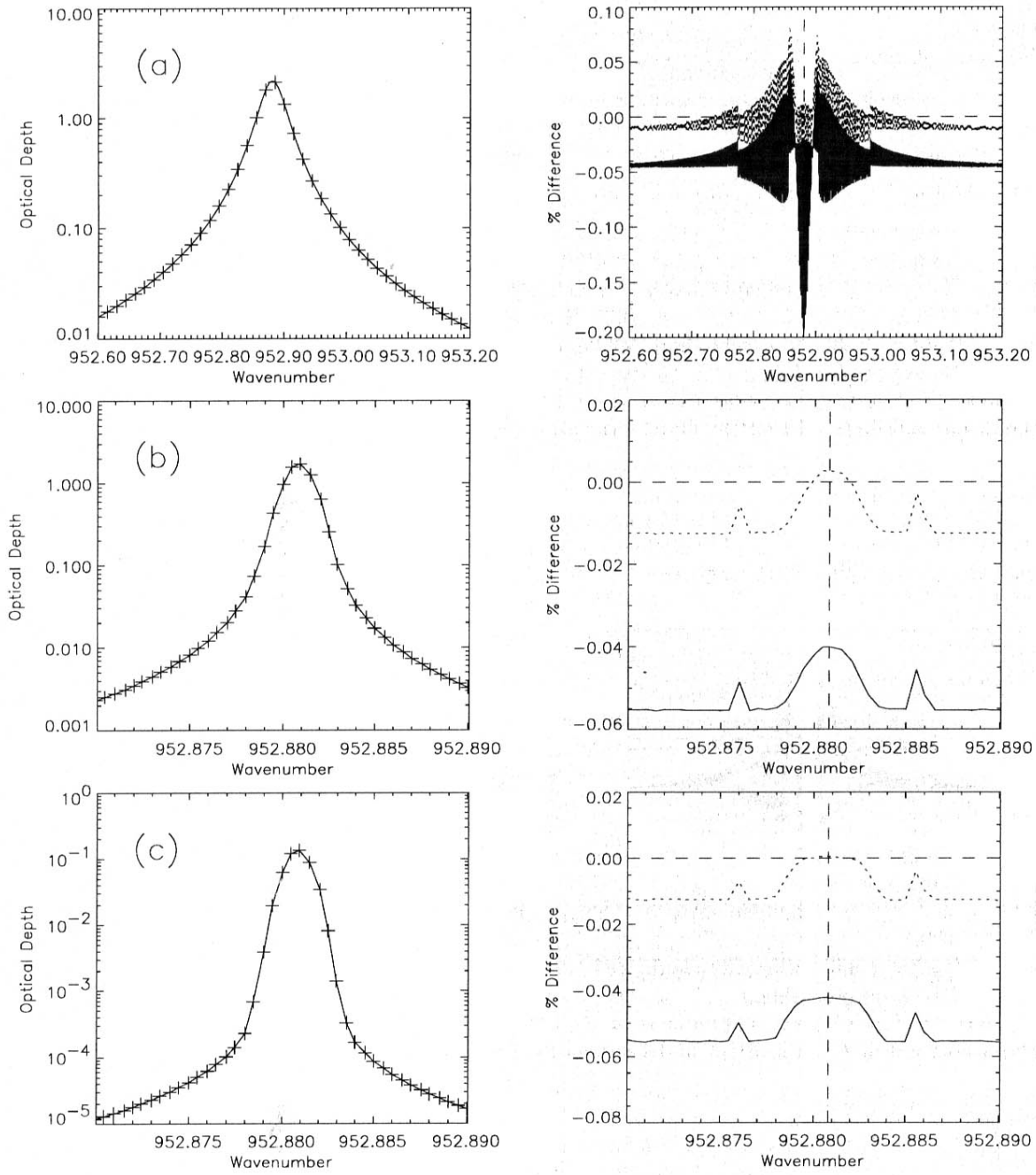

Figure 2: Optical Depth calculations for single CO_2 line in homogeneous path conditions appropriate for (a) Pressure broadening, (b) Mixed region, and (c) Doppler broadening. The solid line represents the RFM calculation and the crosses the OFM calculations (both at 0.0005 cm^{-1} resolution, although only a subset of the OFM points are shown in (a) for clarity). Note that the wavenumber scale in (a) is 3× wider than in (b) and (c). The right-hand plots show the % difference 100(OFM−RFM)/RFM, the dashed lines representing zero and the line centre. The dotted line shows the % difference if the '96 TIPS function is used in the RFM.

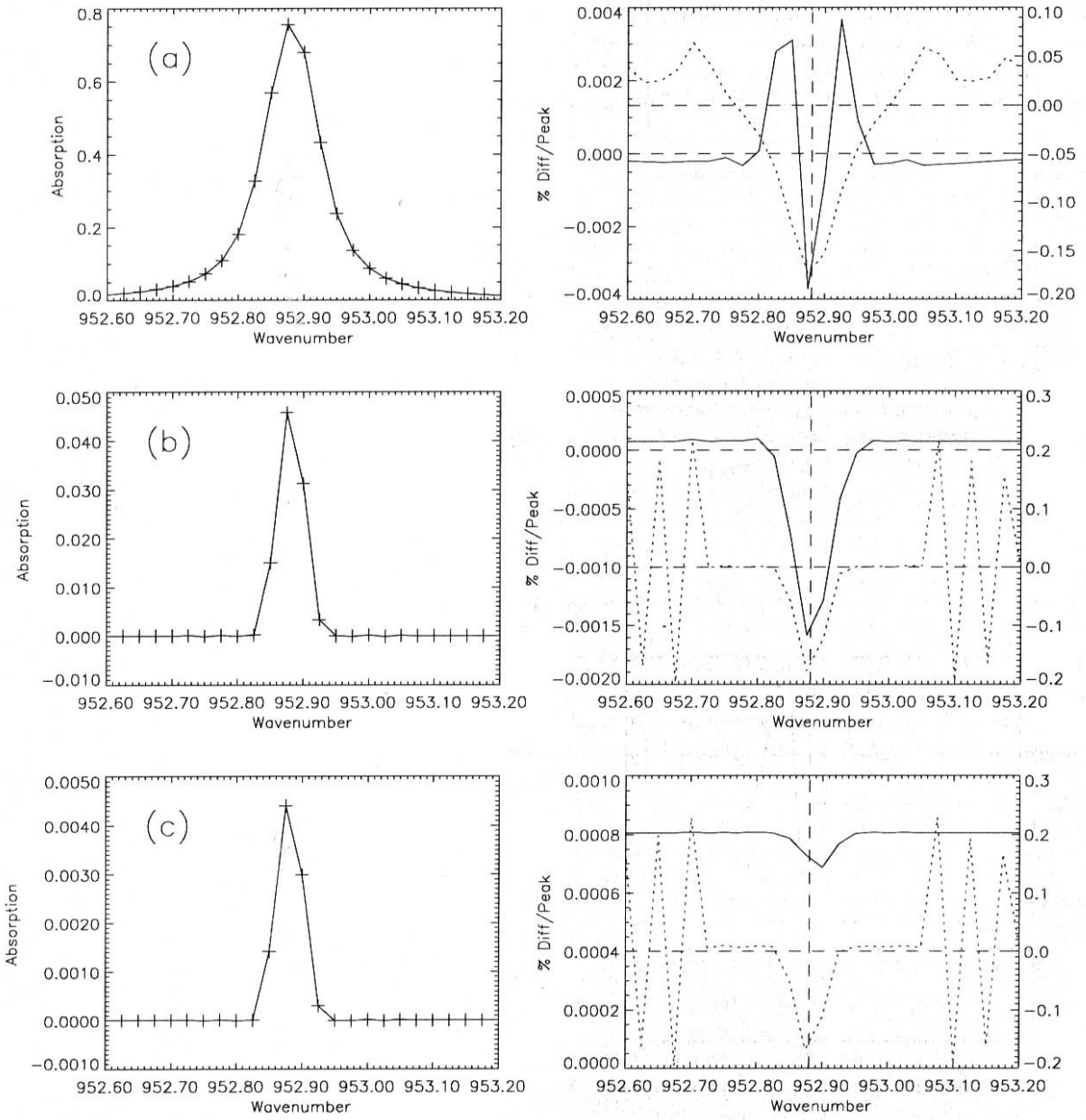

Figure 3: Apodised absorption spectra for the same three cases shown in Fig. 2. The solid line represents the RFM calculation and the crosses a subset of the OFM calculations at 0.025 cm^{-1} resolution, both convolved with the same (IROE) ALS function. The right-hand plots show the difference expressed as a percentage of the peak value (solid line, left axis). The right hand plot (dotted line, right axis) also shows the % peak differences if the RFM calculations convolved with the FFT ALS function. The '96 TIPS data were used for all these RFM calculations.

The apodised absorption spectra are shown in Fig. 3. In this case, the differences are expressed as a % of the peak absorption.

Considering first the comparison when the same (IROE) apodisation function is applied to both OFM and RFM absorption spectra. For the Lorentzian case (a), the apodisation smooths out the oscillations evident in the comparison of optical depth (Fig. 2), but otherwise preserves the general shape of the difference. The % difference in the peak is also reduced as expected from the non-linear relationship between optical depth and absorption, in this case by a factor ~ 10. For the (b) and (c) cases, the ALS convolution unexpectedly inverts the sign of the OFM-RFM difference at the peak. Also, there is a persistent positive offset in the wings due to slightly negative values of RFM absorption (this arises from the RFM convolution of transmission rather than absorption, using a single-precision ALS function), and the inversion of the peak difference is probably a related effect. However, these differences are negligible in absolute terms.

Comparing the OFM results with the RFM spectra convolved with the extended FFT-ALS (which represents a more realistic 'measured' spectrum) the dominant effects are the 0.2–0.3% peak difference plus 'ringing' of 0.2% peak amplitude beyond ± 0.175 cm^{-1} from the line centre: all effects expected from the comparisons between the two ALS functions in section 1.4.

The conclusion is that differences between the OFM and RFM in modelling line shape and convolving with *the same* ALS function lead to absorption spectra differing by less than 0.002% of the peak absorption, which is insignificant compared to the discrepancy of 0.2% peak absorption associated with the modelling of the actual ALS function itself.

3.3 Line Wing Assumptions

Both the OFM and the RFM make various approximations in describing the line shape away from the line centre. To compare the treatment of multiple lines and line wings, optical depth calculations were performed for the H_2O microwindow 1413.9–1416.4 cm^{-1} (which is in the vicinity of several strong lines) for a 250 km homogeneous path under conditions typical of 10 km altitude: $p = 250$ mb, $T = 220$ K, H_2O vmr = 67 ppmv. Four types of calculation were performed, just considering H_2O absorption in all cases:

(a) Using only lines centred in the range 1413.9–1416.4 cm^{-1} (i.e. within the microwindow itself)

(b) Using lines within 1408.9–1421.4 cm^{-1} (microwindow boundaries ± 5cm^{-1})

(c) Using lines within 1388.9–1441.4 cm^{-1} (microwindow boundaries ± 25cm^{-1})

(d) Same as (c) with the addition of the H_2O continuum (defined as accumulation of line wings beyond 25 cm^{-1}).

The results are shown in Fig. 4, once again plotting the optical depth spectra on a logarithmic scale and showing % difference to emphasise the line-wing comparison. The results for (b) are essentially similar to (c) so are omitted for reasons of space.

The superimposed optical depth curves show no major discrepancies between the two models. The difference plots show agreement in optical depth ($\propto$ absorption coefficient k) of the order of 0.5% for (a) and (c), degrading to around 1% when the continuum is added in (d).

The heavy shading at the line peaks in the difference plots is from the oscillations caused by the OFM interpolation, as previously noted in Fig. 2(a).

The large sinusoidal differences, e.g. between 1415–1416 cm^{-1} in (c), have also been noted in comparisons between the RFM and other line-by-line models [12]. These are caused by the RFM method of calculating line wing absorption. Beyond 1–2 cm^{-1} from the line centre (actually defined by the 1 cm^{-1} interval boundaries in the spectrum) the RFM only calculates the absorption coefficient at 3 points/1 cm^{-1} interval. Then accumulated absorption from all 'non-local' lines at these three points is then fitted with a quadratic to obtain the absorption at the intermediate fine grid points.

Generally this procedure works adequately (the same is used in GENLN2 v.3) but, in the presence of a strong line or group of lines centred just outside the 'local' line definition (>1417.0 cm^{-1} for the 1415–6 cm^{-1} interval) the accumulated line-wing contributions are still strongly Lorentzian, and poorly modelled by a quadratic fit:

$$a\nu^2 + b\nu + c \not\approx \frac{S}{\pi} \frac{\alpha_L}{(\nu - \nu_0)^2 + \alpha^2} \tag{12}$$

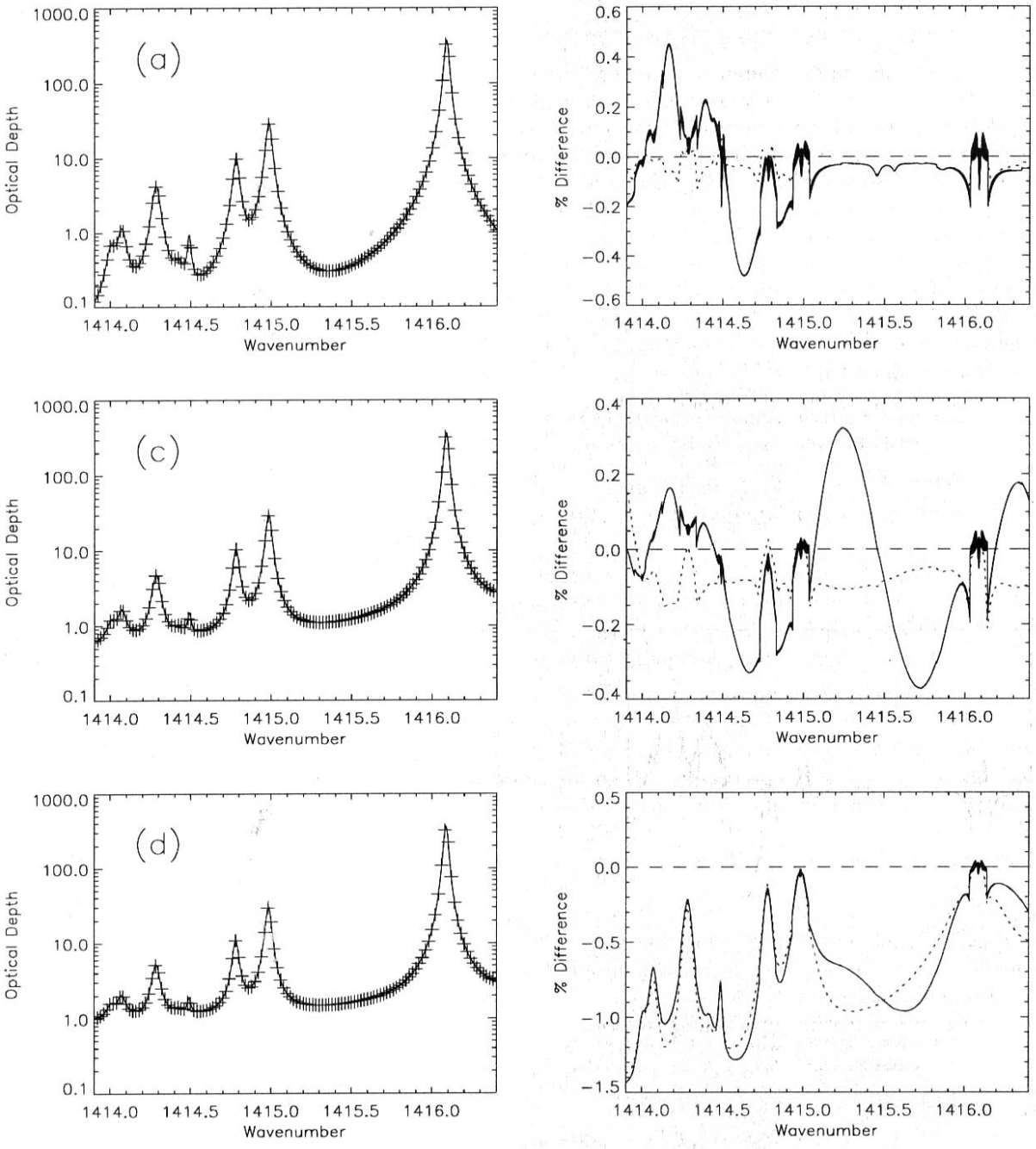

Figure 4: Optical Depth spectra for the 1413.9–1416.4 cm^{-1} H_2O Microwindow considering (a) only H_2O line within the microwindow, (c) H_2O lines centred up to 25 cm^{-1} from the MW edges, (d) also including H_2O continuum. The solid line shows the RFM spectrum and the crosses a subset of the OFM calculations. The solid lines in the right plot show the % difference (OFM−RFM), and the dotted lines show the difference if the RFM calculations are performed using the 'IQD' option (see text). The results for case (b) (edges ± 5 cm^{-1}) are omitted, but are similar to (c).

hence the sinusoidal shape between the three explicitly calculated points at 1415.0, 1415.5 and 1416.0 cm^{-1}.

The obvious solution is to invert the expression on the left side of Eq. 12 to fit an inverse quadratic rather than a quadratic, and the RFM has an option to do this[2]. Using this modification, the OFM-RFM differences in the line-only cases (a), (c), shown by the dotted line in the figure, are reduced to less than 0.1 %. However there is no comparable improvement for the continuum case, because the addition of the essentially-flat continuum distorts the Lorentzian shape to such an extent that it can be equally well fitted by a quadratic or an inverse quadratic.

The OFM and the RFM both use different implementations of the same CKD_21 continuum model [13]. The OFM follows the recommended approach which, for each line, first requires the subtraction of the absorption coefficient evaluated at line centre ± 25 cm^{-1} before adding the continuum term. The RFM approach, derived from GENLN2, is to evaluate the line absorption coefficient normally but then add a modified continuum which represents the original continuum model minus the ± 25 cm^{-1} offsets for each line. In principle, these two approaches should be give the same answer, but differences arise from the application of various empirical functions (primarily to correct for foreign-broadening) to the different continuum terms. The OFM also ignores the self-broadening component whereas this is included by the RFM.

Given the large changes in recent CKD models for this region ($\sim$ factor 2 in absorption), it is unlikely that the actual continuum is known to better accuracy than the observed difference between the RFM and the OFM. As the continuum emission is fitted as part of the retrieval, accurate modelling is not essential in any case.

The conclusions are that there are explainable differences of the order of 1% between the OFM and RFM handling of accumulated line wing absorption coefficients, which, if corrected (e.g. by using the 'IQD' option or exactly the same continuum implementation), leave residual differences of $\sim$0.1%. It is unlikely that these wings contribute significantly to the microwindow radiance or the retrieval error, but this will be tested in section 4.3.

3.4 Full Microwindow Calculations

The previous section dealt with a single species in a single microwindow. This section compares typical MIPAS microwindows for all 6 target species (including CO_2 for the p, T retrieval), including any 'cross-contamination' of lines of one species in another microwindow. For convenience, the path conditions were set the same (equivalent to around 40 km altitude) for all microwindows, i.e. effectively all viewing the same homogeneous path. The selected microwindows and conditions were:

Pressure=2.5 mb, Temperature=250 K, Path Length=250 km

(a)	PT012A MW	700.85–701.1 cm^{-1}	CO_2 = 330 ppmv
(b)	CH440A MW	1355.0–1356.75 cm^{-1}	CH_4 = 0.6 ppmv
(c)	N2O20A MW	1879.35–1880.3 cm^{-1}	N_2O = 0.05 ppmv
(d)	O3014A MW	763.5–764.65 cm^{-1}	O_3 = 7.0 ppmv
(e)	HNO08A MW	888.5–891.2 cm^{-1}	HNO_3 = 0.0005 ppmv
(f)	H2O17A MW	1413.9–1416.4 cm^{-1}	H_2O = 5.0 ppmv

The results, expressed as ALS-convolved absorption spectra (using just the IROE ALS function), are shown in Fig. 5, together with a % difference to highlight discrepancies in low-absorption regions of the microwindows.

The plots show no gross discrepancies between the two models, i.e. the crosses representing the OFM results lie on the solid line representing the RFM results. The effect of the CO_2 χ-factor in (a) will be discussed in section 5.4.

Comparing the % difference results (dashed lines) several dips are observed, notably in the N_2O microwindow (c) at 1879.5 cm^{-1}, in the O_3 microwindow (d) at 763.55 cm^{-1}, and various points in the H_2O microwindow (f). The OFM uses a dedicated line database for each microwindow (supplied by IMK) which is derived from HITRAN '96 but includes only the lines determined to be significant for computing the microwindow radiance. The dips have been identified as arising from lines present in the full HITRAN '96 database (as used by the RFM) but excluded from the OFM microwindow database.

[2]The 'IQD' ('Inverse Quadratic Fit') option has not been generally used in these intercomparisons but *has* been used to generate the set of reference spectra for the OFM/ORM tests

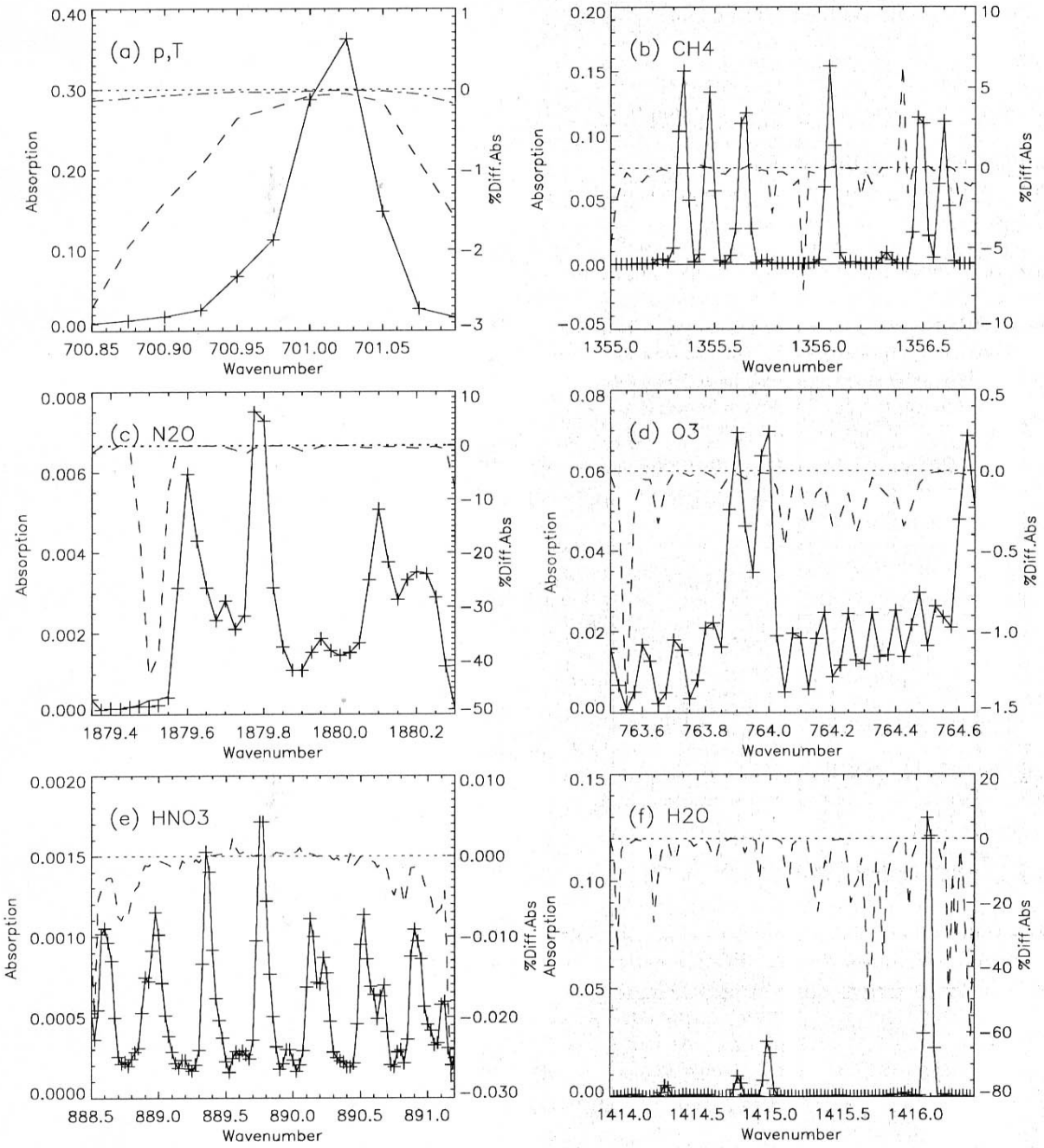

Figure 5: ALS-convolved Absorption spectra for selected MIPAS microwindows (see text for details). The solid line shows the RFM calculation, the crosses the OFM calculation (both at 0.025 cm^{-1} resolution) and the dashed line (right axis) the % difference in absorption. The dot-dash line in (a) shows the effect of including the CO_2 χ-factor in the RFM calculation.

Such features are expected when they lead to negligible differences in *absolute* absorption, which is true of most cases here. However, the missing line in the N_2O microwindow (c) (actually an O_3 line), is apparently more problematic, causing a visible difference between the RFM and OFM absolute absorption results. However, these path conditions are not representative of the nominal altitude range for this microwindow, so this need not imply a problem with the microwindow database line-rejection criteria.

The general conclusion from this test is that the OFM and the RFM agree to better than 1% near the major absorption features. The impact of these differences on radiance measurements will be investigated in section 4.3.

4 Limb Spectral Calculations

The final series of tests compare limb spectral calculations, combining the results of the ray-tracing calculations in section 2 with the homogeneous path spectral calculations of section 3. For these tests it was necessary to modify the OFM to use profiles based on the US76 layering (normally it constructs profiles based on the 3 km spacing used for the retrieval) and also to suppress the internal hydrostatic adjustment which would otherwise lead to discrepancies (see Table 2) between the OFM pressure and RFM pressure which is taken directly from the US76 atmosphere.

4.1 Limb Absorption

This section examines the single CO_2 line used in section 3.1 viewed at the three limb tangent heights used in section 2.1, i.e.,

(a) 10 km tangent path

(b) 40 km tangent path

(c) 60 km tangent path

Absorption spectra calculated for all three cases (on the Fine Grid, without ALS and FOV convolutions) are shown in Fig. 6, with differences are expressed as a percentage of the peak absorption. The dotted lines in each plot show the difference if the RFM calculation is performed using the '96 TIPS data instead of the '92 TIPS.

The 10 km case (a) again shows the oscillations due to the OFM variable grid spacing used at low altitudes (see Fig. 2(a)).

The difference plot for the 40 km case (b) is consistent with the equivalent homogeneous path difference (Fig. 2(b)) given that the line centre is much higher (opaque) in this case, but the inversion in case (c) is unexplained: it is too large to arise from the absorber amount discrepancies identified in section 2.2 (Table 5).

For a single CO_2 line, the limb absorption calculations agree to approx. 0.02% of the peak absorption for strong lines ($a_{\max} \sim 1$), and around 0.2% for weak lines ($a_{\max} \sim 0.25$). Approximately 25% of these differences can be removed by use of the '96 TIPS in the RFM calculation.

4.2 Limb Radiance

Radiance spectra (in units of $\mathrm{nW/(cm^2.sr.cm^{-1})}$) were calculated for the single CO_2 line and 10 km path used in the previous section with various convolutions and alternatives to the 'standard' RFM calculation (i.e. '92 TIPS, IROE ALS function and 9-pt FOV convolution).

(a) No convolution (alternative: '96 TIPS data)

(b) ALS convolution (alternative: FFT ALS)

(c) FOV and ALS convolution (alternative: 12-pt FOV convolution)

The FFT ALS was discussed in section 1.4, the '96 TIPS and FOV functions will be discussed in section 5. The 10 km tangent path is chosen to provide a severe test of the FOV convolution since the line shape is changing rapidly with height at low altitudes. The results are presented in Fig. 7 with differences expressed as absolute radiance. For comparison, NESR/4 for this region (band A) is 12.5 $\mathrm{nW/(cm^2.sr.cm^{-1})}$.

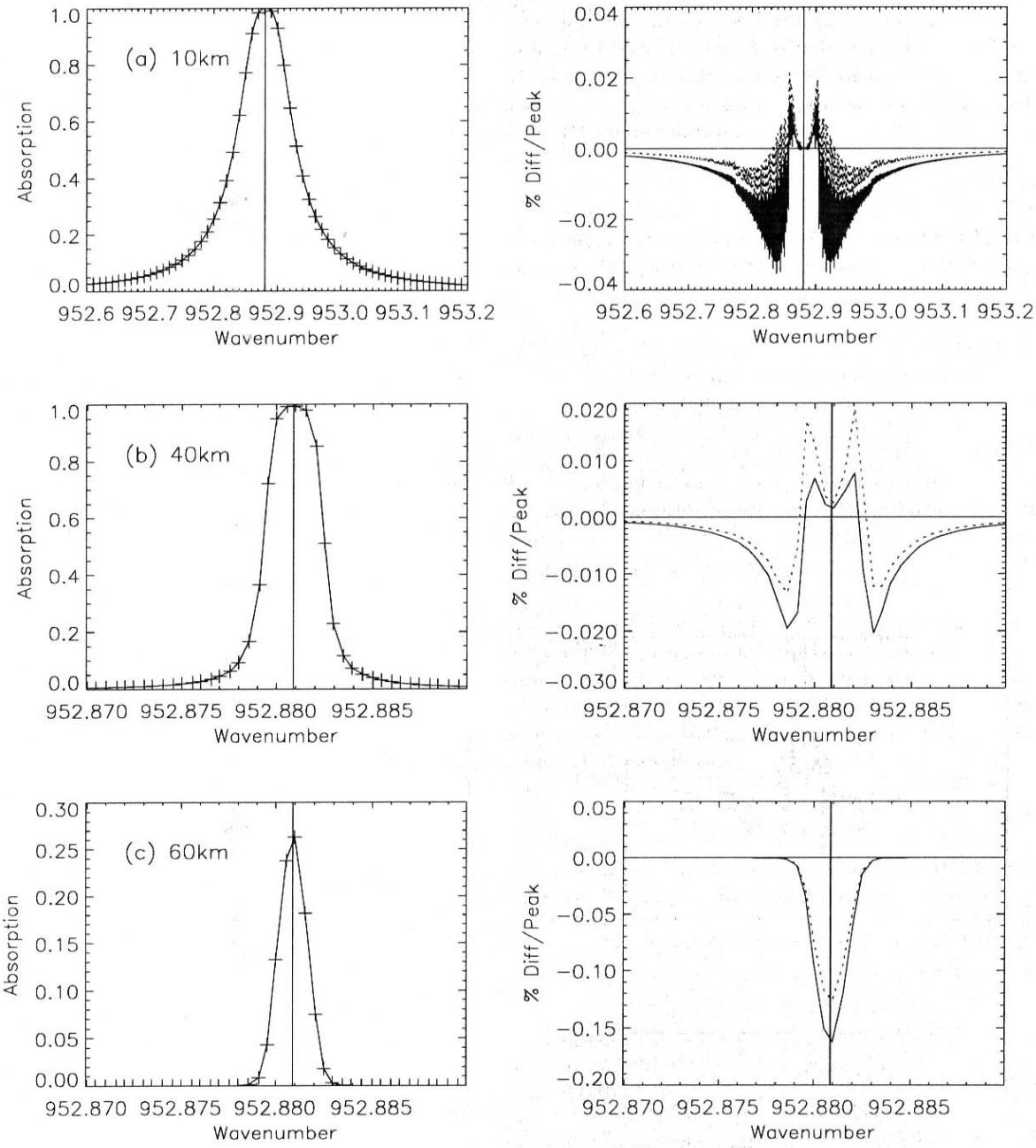

Figure 6: Unconvolved absorption spectra for the CO_2 line in Fig. 2 for limb paths at (a) 10 km, (b) 40 km and (c) 60 km tangent heights. In the left hand plots, the RFM calculations are shown by the solid line and the OFM calculations by the crosses. All spectra are 0.0005 cm^{-1} resolution, but only a subset of OFM points are shown in (a). The right hand plots show the % difference as a fraction of the peak absorption. The dotted line shows the difference if the '96 TIPS data are used in the RFM.

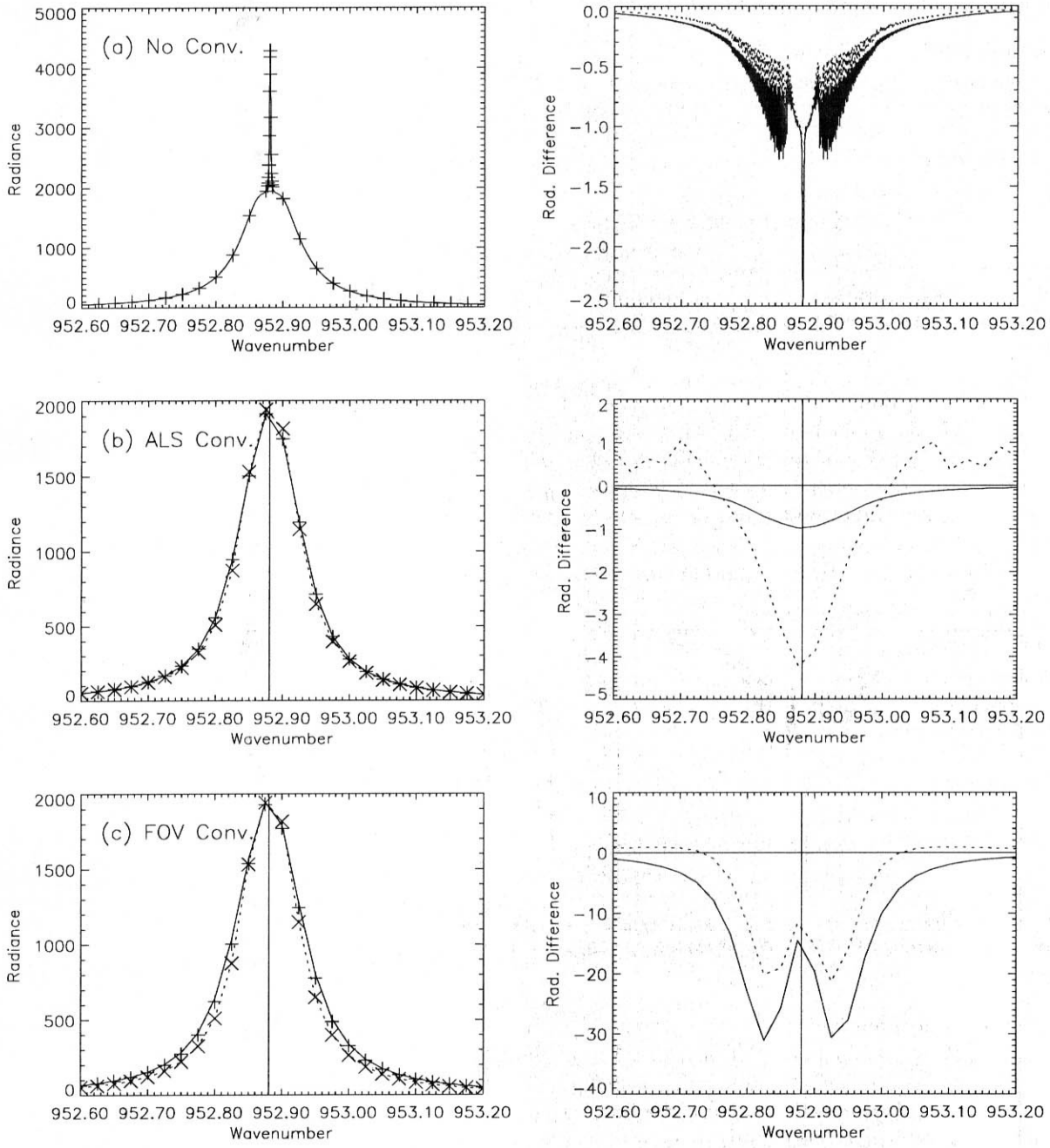

Figure 7: Limb radiance spectra (nW/cm^2.st.cm^{-1}) for the 10 km tangent height CO_2 line in Fig. 6, (a) unconvolved (0.0005 cm^{-1} grid), (b) with ALS convolution (0.025 cm^{-1}), and (c) with both ALS and FOV convolution (0.025 cm^{-1}). In the left hand plots, the RFM calculations are shown by the solid line and the OFM calculations by + crosses. In plot (a) only a subset of the OFM points are shown. In plots (b) and (c), the results from (a) sampled at 0.025 cm^{-1} are superimposed for comparison (as dotted line and and $\times$ crosses). The right hand plots show the radiance difference (OFM-RFM) for each case, with the solid lines showing the difference using RFM v2. In (a), the dotted line shows the difference if the '96 TIPS data are used. In (b) the dotted line shows the difference if the RFM radiances are convolved with the FFT ALS instead of the standard IROE function. In (c) the dotted line shows the difference if the RFM FOV convolution is performed using a 12-pt function instead of the standard 9-pt function.

The basic unconvolved limb radiance calculation (a) can be compared with the unconvolved limb absorption calculation in Fig. 6(a). The typical discrepancies of 0.5 nW in the wing correspond to 0.025% of the peak radiance, so can be explained entirely in terms of the absorption discrepancies. The improvement from using the '96 TIPS is also consistent.

Since the line is quite broad, it is expected that the ALS convolution just smooths oscillations without any significant change in shape or magnitude, and this appears to be the case in (b) (solid line). Using the FFT line shape (dotted line) produces the expected 0.2% reduction at the peak, but the width of the line smooths out the oscillations beyond ± 0.175 cm^{-1} evident in Fig. 1.

The addition of a FOV convolution (c) produces the greatest discrepancy between the two models. Since this actually is a combined FOV+ALS convolution, a 'perfect' FOV match would reduce to the difference shown in (b), but the observed differences are 20–30 times larger. Running the RFM at a higher FOV resolution (12 pt instead of 9 pt) removes some of this difference (even higher resolutions make little additional difference) and the remainder is presumably due to the OFM FOV convolution.

The conclusions are:

1. The radiative transfer calculation itself introduces no significant additional error (for a single absorber) compared to the absorption/transmission calculation.

2. The alternative FFT ALS function (section 1.4) corresponds to discrepancies of around 0.2% of the peak radiance (applicable to any isolated line).

3. The FOV convolution (for this particular CO_2 line at 10 km) leads to discrepancies of 1.5%, of which about 0.5% is due to the RFM and the remainder presumed due to the OFM. This is a significant problem, which is investigated further in section 5.2

4.3 Microwindow Radiance

The final test is to compare fully-convolved limb-radiance calculations for the typical set of MIPAS microwindows defined in section 3.4, effectively simulating the operational Forward Model calculations. For this test realistic tangent heights were selected within designated range for each microwindow (in section 3.4 the same homogeneous path had been used for all 6 microwindows).

Case	Microwindow	Target	Wavenumber Range	Band	NESR	Tan. Ht.
(a)	PT012A	p, T	700.85–701.1	A	50 nW	40 km
(b)	CH440A	CH_4	1355.0–1356.75	B	20 nW	40 km
(c)	N2O20A	N_2O	1879.35–1880.3	D	4.2 nW	10 km
(d)	O3014A	O_3	763.5–764.65	A	50 nW	40 km
(e)	HNO08A	HNO_3	888.5–891.2	A	50 nW	10 km
(f)	H2O17A	H_2O	1413.9–1416.4	B	20 nW	10 km

The results are plotted in Fig. 8.

For the CH_4 (b) and O_3 (d) microwindows (both 40 km tangent heights) the differences are well within the NESR/4 criterion.

For the p, T (a) and HNO_3 (e) microwindows the maximum differences are comparable with NESR/4.

For the H_2O (c) and N_2O (f) microwindows the differences are generally larger than the NESR/4 (for the N_2O microwindow the difference is actually >NESR).

These results will be analysed further in the following sections.

5 RFM Modifications

The results of section 4.3 showed significant discrepancies between the OFM and RFM v2 radiance calculations for four of the six microwindows. These four include the three 10 km tangent height views (N_2O, HNO_3 and H_2O), the fourth being the p, T microwindow at 40 km tangent height. No significant differences were identified for the other two 40 km tangent height microwindows (CH_4 and O_3).

Three possible causes for these differences have already been noted from previous tests: the use of different TIPS data between the RFM and the OFM (Fig. 2) the FOV convolution (Fig. 7(c)), and the inclusion of

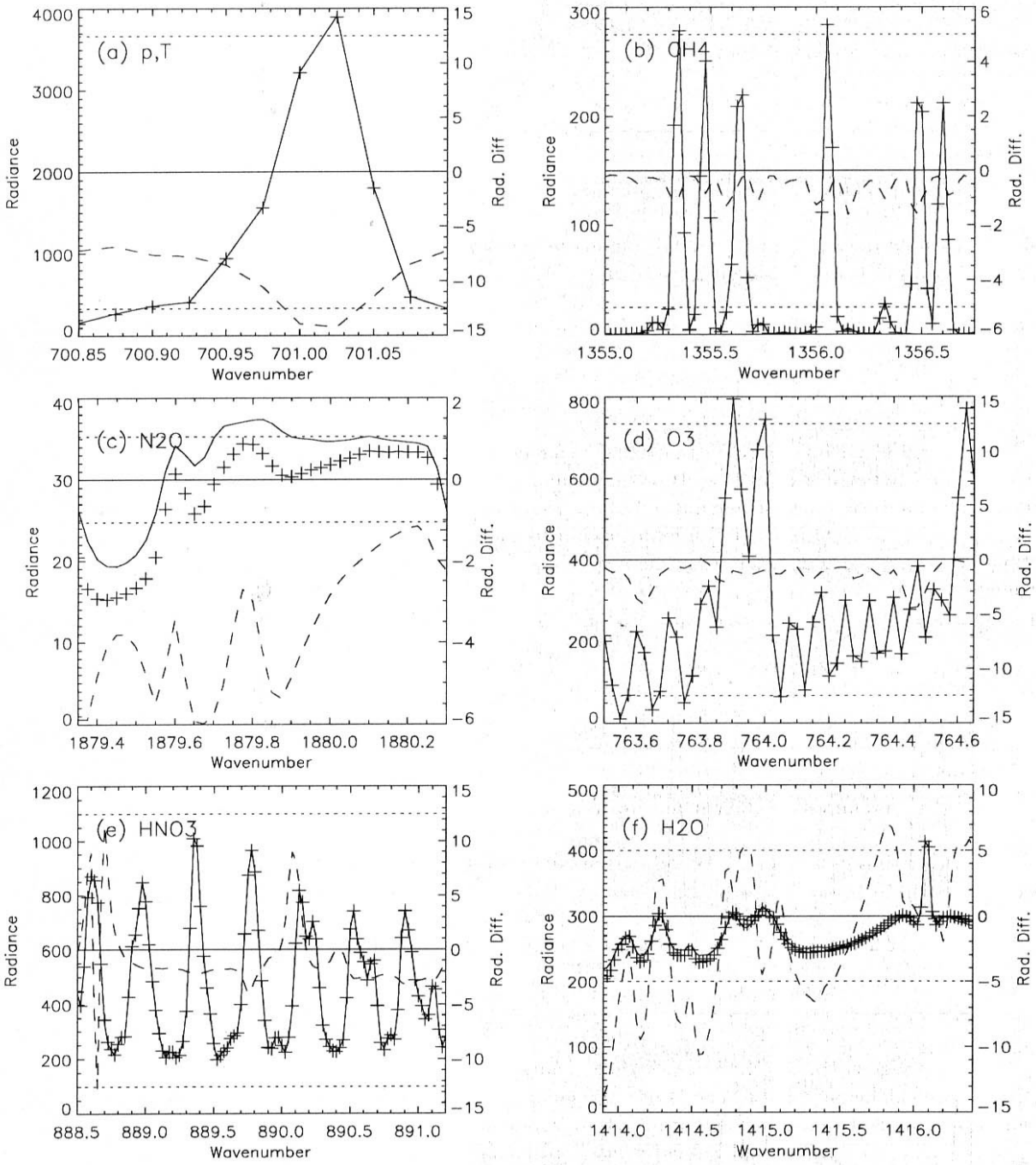

Figure 8: Limb radiance spectra ($nW/cm^2.st.cm^{-1}$) for 6 selected microwindows using RFM v2. The radiances (left hand axis) are shown by the solid line (RFM) and the crosses (OFM). The OFM-RFM differences (right hand axis) are shown by the dashed line. The dotted lines show the $\pm$NESR/4 criterion appropriate for each microwindow. All spectra are at 0.025 cm^{-1} resolution.

the CO_2 χ-factor (Fig. 5(a)). Another cause has also been identified, associated with the RFM radiative-transfer algorithm. These four effects will be analysed in detail in the following sections, but to establish their relative importance, Fig. 9 shows the contribution of each to the OFM-RFM differences seen in Fig. 8.

5.1 Radiative Transfer Algorithms

The OFM and the RFM handle the radiative transfer equation in different ways: the OFM assumes that all species are in local thermodynamic equilibrium (LTE) so that emission is characterised by the Planck function, whereas the RFM assumes separate source functions for each absorber for consistency with non-LTE calculations.

The general form for calculating the radiance R from a path s containing several absorbers i with different (i.e. non-LTE) source functions J_i is:

$$\int dR = \int_{\text{path}} \tau \left(\sum_i J_i \frac{da_i}{ds} \right) ds \tag{13}$$

where a_i is the absorption due to species i. Within the RFM this is implemented as a summation of layer radiance contributions δR, each layer radiance being calculated as the sum of absorber contributions:

$$\delta R = \tau \sum_i J_i \delta a_i \tag{14}$$

where τ is the transmission from the layer to the satellite and δa_i are the layer absorptions due to each species, calculated from the absorption coefficient k_i and layer absorber amount δu_i (Eq. 7) using:

$$\delta a_i = 1 - \exp(-k_i \delta u_i) \tag{15}$$

In LTE, all the source functions reduce to the Planck Function, B, which can then be removed from the summation[3], leaving:

$$\delta R = \tau B \sum_i \delta a_i \tag{16}$$

However, if it is assumed from the start that LTE applies, then the radiative transfer equation (Eq. 13) would be written:

$$\int dR = \int_{\text{path}} \tau B \frac{da}{ds} ds \tag{17}$$

where a is now the total absorption from all species. This is implemented in the OFM as:

$$\delta R = \tau B \delta a \tag{18}$$

where δa is the total layer absorption, defined as:

$$\delta a = 1 - \exp\left(- \sum_i k_i \delta u_i \right) \tag{19}$$

The RFM uses Eq. 14 whereas the OFM uses Eq. 18, designated the 'LTE' algorithm. Essentially the difference is whether the different absorber contributions are summed before or after the exponentiation. For a single absorber the two forms are identical. For multiple absorbers the results also converge provided that there is only one *significant* absorber in the layer. Where two (or more) absorbers have significant absorption the results differ, the 'LTE' form being the more accurate.

If the RFM is modified to use the 'LTE' form (shown by the dotted lines in Fig. 9), this significantly improves the comparison with the OFM in the (a) p, T and (c) N_2O microwindows, and has a noticeable effect in the (d) O_3 and (f) H_2O microwindows. There is little change in the CH_4 and HNO_3 microwindows, presumably because the emission is almost entirely from the target species.

[3] In fact, the RFM uses Planck functions characterised by the individual Curtis-Godson temperatures for each absorber, but the differences are usually negligible

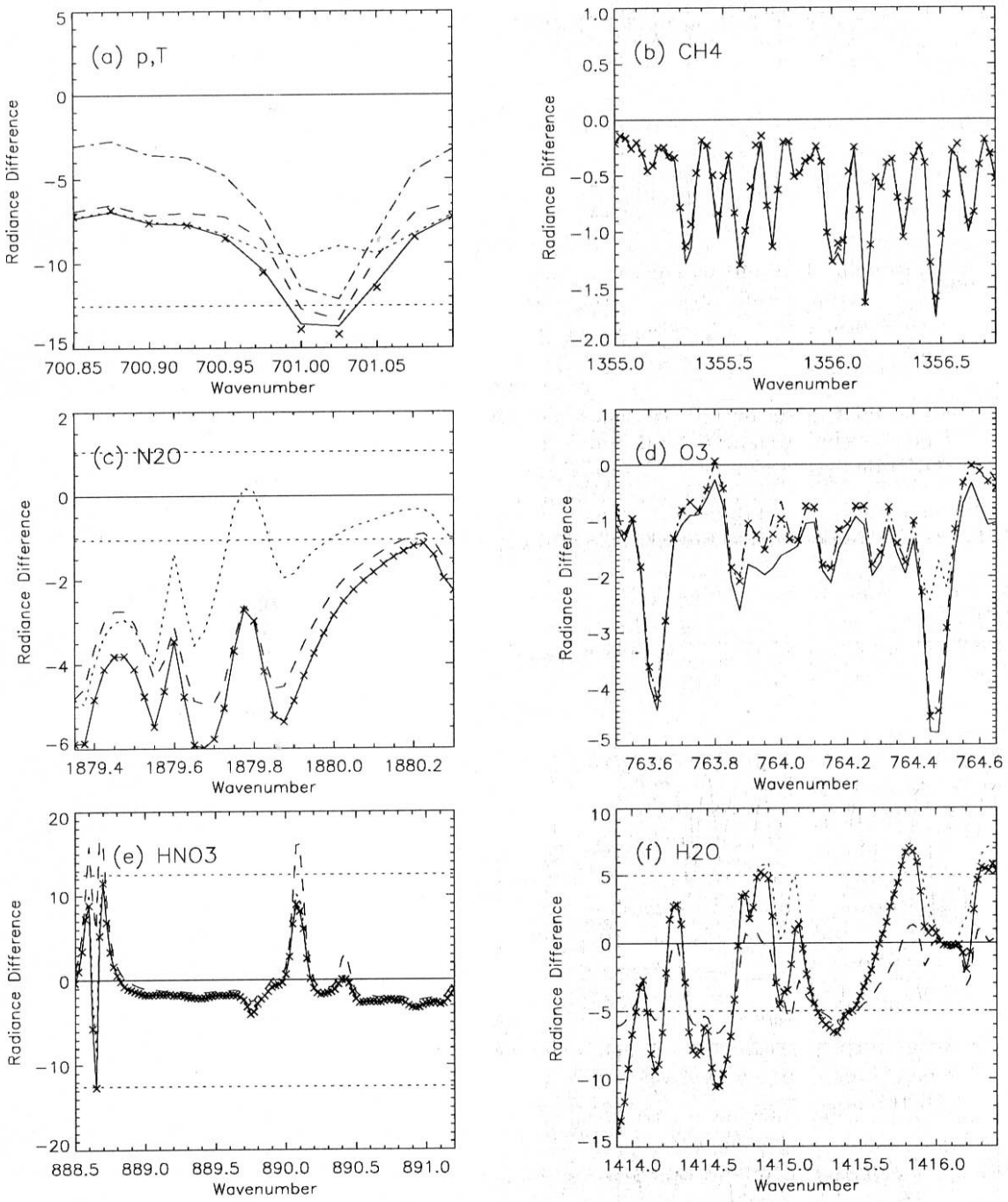

Figure 9: Changes to the OFM-RFM difference spectra in Fig. 8 (shown here as crosses), resulting from various modifications to the RFM radiances: 'LTE' radiative transfer (dotted line), 12 pt FOV convolution (dashed line), '96 TIPS (solid line) and the CO_2 χ-factor (dot-dash, in (a) only). The horizontal dotted lines show the $\pm$NESR/4 criterion for the microwindow if within the plot range.

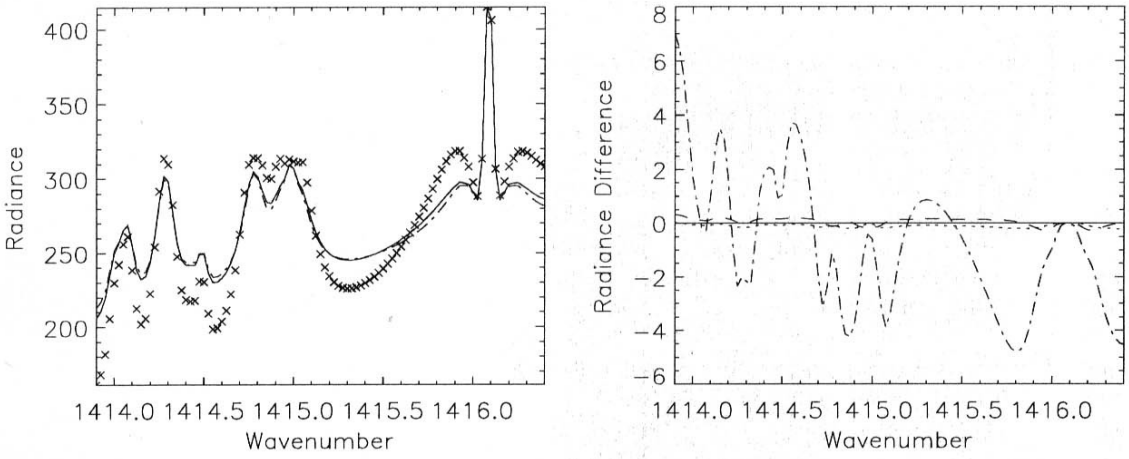

Figure 10: Effect of different numbers of points used within the RFM to perform the FOV convolution. The left plot shows limb radiance calculations for the H_2O microwindow at 10 km tangent height (H_2O lines only). The different lines represent different numbers of points: 9 pts (dot-dash), 12 pts (dashed), 15 pts (dotted) and 21 pts (solid), with the 10 km point-FOV radiances shown by crosses for comparison. The right plot shows differences from the 21 pt radiances.

5.2 Field-of-View Algorithms

Both the OFM and RFM assume the MIPAS field-of-view (FOV) has a trapezoidal response function (base 4 km, top 2.8 km), and simulate the effect of the finite FOV by convolving this function $\Phi(z'-z)$ with point-radiances $R(z')$:

$$R_{\text{fov}}(z) = \int \Phi(z'-z)R(z')\,dz' \tag{20}$$

However, the OFM and the RFM implement this convolution using quite different numerical algorithms.

The RFM calculates the point-FOV radiances at (typically) 9 different elevations (~0.5 km spacing) and performs the convolution by assuming the radiance and FOV function vary linearly with altitude between each point [14].

The OFM approach is to use fewer points but fit the radiance profile with a higher-order polynomial. Usually this means 3 points (at the nominal tangent altitude and ±3 km) and assume a quadratic variation with altitude, but for H_2O microwindows in the troposphere 5 points are used (1.5 km spacing) and fitted with a quartic [6].

From this, one would expect the RFM 9-pt function to be an improvement on the OFM quadratic fit and comparable with the quartic fit.

Tests were performed, running the RFM at higher FOV resolutions: 12 points, corresponding to approximately 0.4 km spacing, 15 pts (~0.3 km) and 21 pts (~0.2 km). The results should converge once 'adequate' resolution has been reached. The H_2O microwindow at 10 km tangent height was chosen as this appears to exhibits the most sensitivity to FOV representation (due to the steep gradient in upper tropospheric water vapour). The results are shown in Fig. 10.

This shows an improvement of several nW in going from a 9-pt to a 12-pt representation, but thereafter only limited increases in accuracy (<0.5 nW). This suggests that, for this particular microwindow at least, the 12-pt FOV representation is optimal.

The test was also performed for the CO_2 line shown in Fig. 7(c), and again a significant improvement was found in changing from 9 pt to 12 pt, with only negligible improvement at higher resolutions.

Fig. 9 (dashed line) shows that switching to a 12 pt FOV results in a major improvements for the (f) H_2O microwindow limb radiance calculations and some improvement for the (a) p, T and (c) N_2O microwindows.

There is very little change in the (b) CH_4 and (d) O_3 microwindows since these are at high altitudes where the line shape does not vary significantly with tangent height. The (e) HNO_3 comparison actually worsens, but since the 3 spikes actually correspond to H_2O lines this may just represent the fact that these are now more accurately modelled than previously (the OFM only models H_2O lines outside the H_2O microwindows with a quadratic, so is likely to be inaccurate).

5.3 Partition Functions (TIPS)

The HITRAN line database also includes sets of coefficients for the calculation of the temperature dependence of the Total Internal Partition Sum (TIPS) $Q(T)$ for each molecule/isotope, calculated by Gamache.

$$Q(T) = a_0 + a_1 T + a_2 T^2 + a_3 T^3 \tag{21}$$

This is then applied as a scaling factor to the line strength (nominally measured at T=296 K).

The RFM v2 uses the TIPS functions from the '92 HITRAN data whereas the OFM uses values taken from the '96 HITRAN data (with the exception of HNO_3, which will be explained in section 6.1).

Modifying the RFM to use the '96 TIPS for all species other than HNO_3 has little effect on the microwindow limb radiance calculations (only noticeable in Fig. 9 in the (a) p, T and (d) O_3 microwindows), but did show that this was the dominant component of the optical depth difference in section 3.1 (Fig. 2).

5.4 χ-Factor for CO_2

CO_2 line wings are known to be sub-Lorentzian (e.g. [15]) and this is usually modelled by multiplying by an empirical function: the χ-factor. The effect is negligible (i.e. χ-factor $\simeq 1$) close to the line centre, hence invisible in the earlier Voigt line-shape comparisons using the single CO_2 line (sections 3.1,4.1), but in the p, T microwindow calculations (sections 3.4,4.3) a large number of CO_2 line-wings are included and the effect becomes significant.

The RFM v2 has the capability of applying the CO_2 χ-factor, but it was originally decided to use the pure Voigt line shape for all RFM calculations for this intercomparison. However, the OFM calculations *did* use the χ-factor. Since this is a 'continuum-like' component, in practice it should make little difference to the p, T retrieval since an arbitrary continuum term will also be fitted as part of the retrieval.

Fig. 3.4(a) showed that this explains almost all the % difference in absorption: the bending in the % difference curve being equivalent to a positive offset in the RFM calculation due to the assumption of Lorentzian (=Voigt) line wings. Fig. 9 suggests that this also explains much of the radiance difference in the low emission part of the microwindow (Fig. 8) but is less significant in explaining the peak emission discrepancy (the part actually outside the NESR/4 limit), which is largely due to the RFM radiative transfer algorithm.

5.5 Microwindow Radiances with Modified RFM

The RFM microwindow radiance spectra of section 4.3 have been recalculated with four modifications:

1. use of 'LTE' radiative transfer algorithm instead of non-LTE.
2. use of 12-pt FOV representation instead of 9-pt
3. use of '96 TIPS instead of '92 TIPS (except HNO_3)
4. use of the CO_2 χ-factor in the p, T microwindow calculations

This represents the removal of all known RFM error contributions to the difference, leaving either the unknown or OFM contributions. The new results are replotted in Fig. 11.

Compared to the previous results (Fig. 8) this shows that the (a) p, T microwindow results are now within the NESR/4 criterion, and that the (c) N_2O and (f) H_2O results have improved (although still not entirely within the NESR/4 criterion). This also shows that the (e) HNO_3 discrepancies associated with water vapour lines have worsened, as expected from the results of section 5.2.

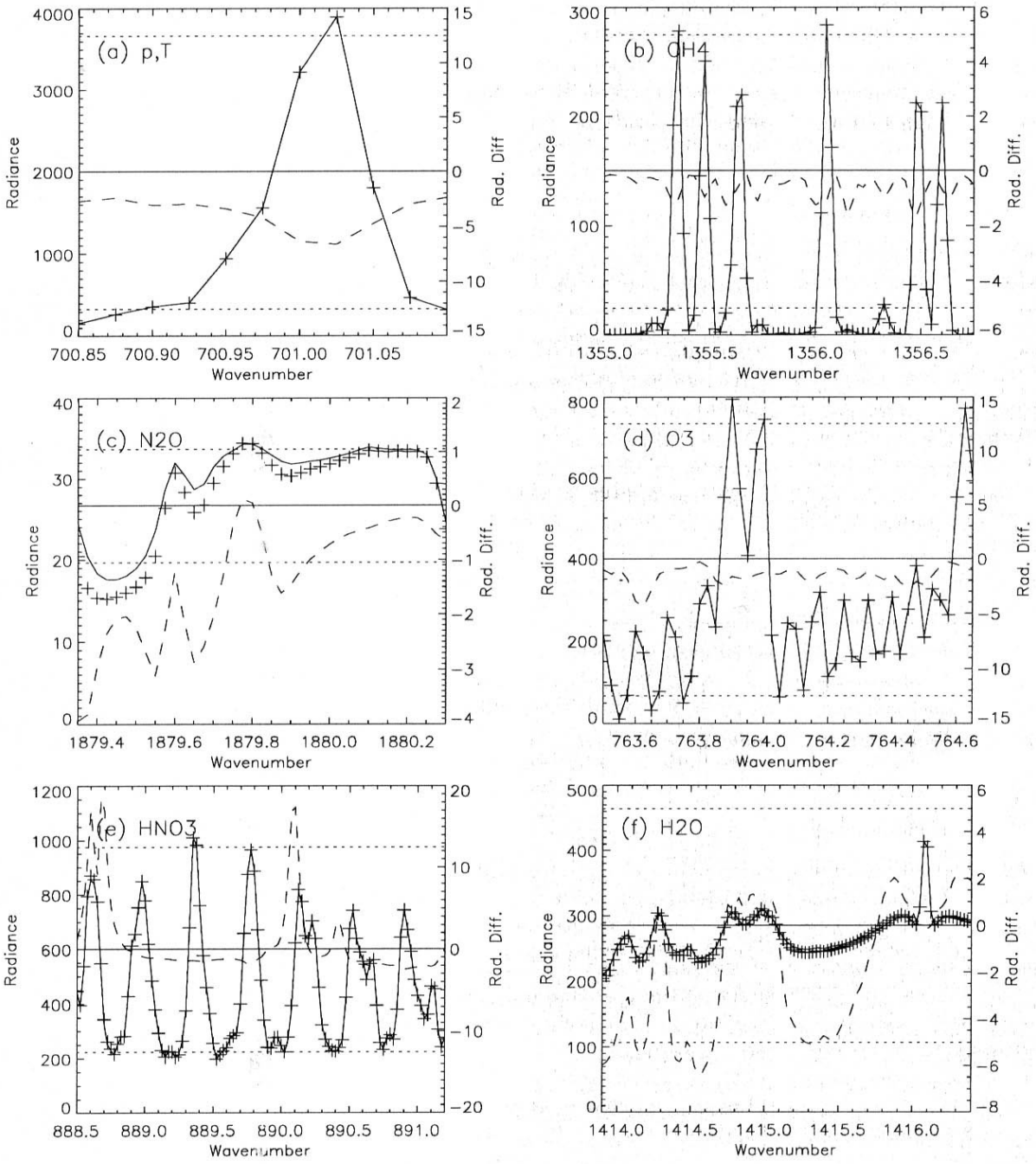

Figure 11: As Fig. 8, except comparing the OFM-RFM having modified the RFM to remove known error contributions to the difference.

6 OFM Modifications

The OFM results presented so far in this study have all been from the latest development version of OFM, which will shortly be delivered as 'Version 2'. This version incorporates various modifications to the OFM v1 to correct problems that have been identified during the course of this study. The modifications were:

1. Replace the '96 TIPS for HNO_3 with the '92 HNO_3 data.
2. Remove the χ-factor from the H_2O lines
3. Correct the altitude coverage for the microwindow calculations

To illustrate the impact of these modifications, Fig. 12 shows the results of OFM v1 calculations compared with the OFM v2.

6.1 TIPS data for HNO_3

During this study, it was realised that the '96 TIPS function for HNO_3 was just the theoretical rotational component,

$$Q_{\text{rot}}(T) = \left(\frac{296}{T}\right)^{\frac{3}{2}} \tag{22}$$

Apparently this is because there has been a problem determining a series of coefficients (Eq. 21) that adequately fit the data over the full temperature range 70–500 K (D. Edwards, pers. comm.), although it may be possible to derive a valid set over a reduced temperature range for atmospheric applications.

Just using the rotation component turns out to be a poor approximation for the more-complete theoretical form (J.-M. Flaud, pers. comm.) which also includes the vibrational component:

$$Q(T) = \left(\frac{296}{T}\right)^{\frac{3}{2}} \prod_{i=1,9} \frac{1}{1 - \exp -(hc\nu_i/kT)} \tag{23}$$

where ν_i (cm^{-1}) are the energies of the first 9 vibrational states. The '92 TIPS gives much better agreement with Eq. 23 so will continue to be used by the OFM and RFM until new coefficients become available.

Fig. 12(e) shows considerable radiance differences, correlated (as expected) with the HNO_3 line shape. Line strengths calculated using the '96 TIPS would be reduced by ~10% compared to the '92 TIPS, which would be expected to translated into a 10% error in retrieved vmr.

This problem was noticed when comparing the HNO_3 microwindow absorption spectra (section 3.4, Fig. 5(e)).

6.2 χ-Factor for H_2O

The original OFM applied a χ-factor to the H_2O Voigt line shape. However, this is already accounted for by the CKD continuum model (which is intended to be applied to lines calculated using just the Voigt line shape) so if the continuum is included in the OFM calculations the χ-factor would effectively be applied twice. Fig. 12 shows the original OFM calculations have larger radiances associated with the line wings (i.e. dips in the H_2O spectrum) of the order of 5 nW, equivalent to a 2% radiance error in these regions.

The problem was noticed when comparing the line wings (section 3.3, Fig. 4).

6.3 Altitude Coverage

The microwindow database generated by IMK assigns an 'altitude coverage' to each line. In the original version of the OFM this was interpreted as the altitude range over which the line needs to be included in the absorption calculations. The altitudes assigned by IMK, however, refer to the *tangent height* range for which the line needs to be considered, on the assumption that the absorption calculations would then include the line at all atmospheric levels up to the top of the model. Thus the OFM v1 started excluding lines at lower altitudes than intended.

The IMK definition cannot be simply incorporated into the OFM because of the way in which the OFM calculates absorption coefficients for each layer for the lowest limb view, then re-uses these coefficients for

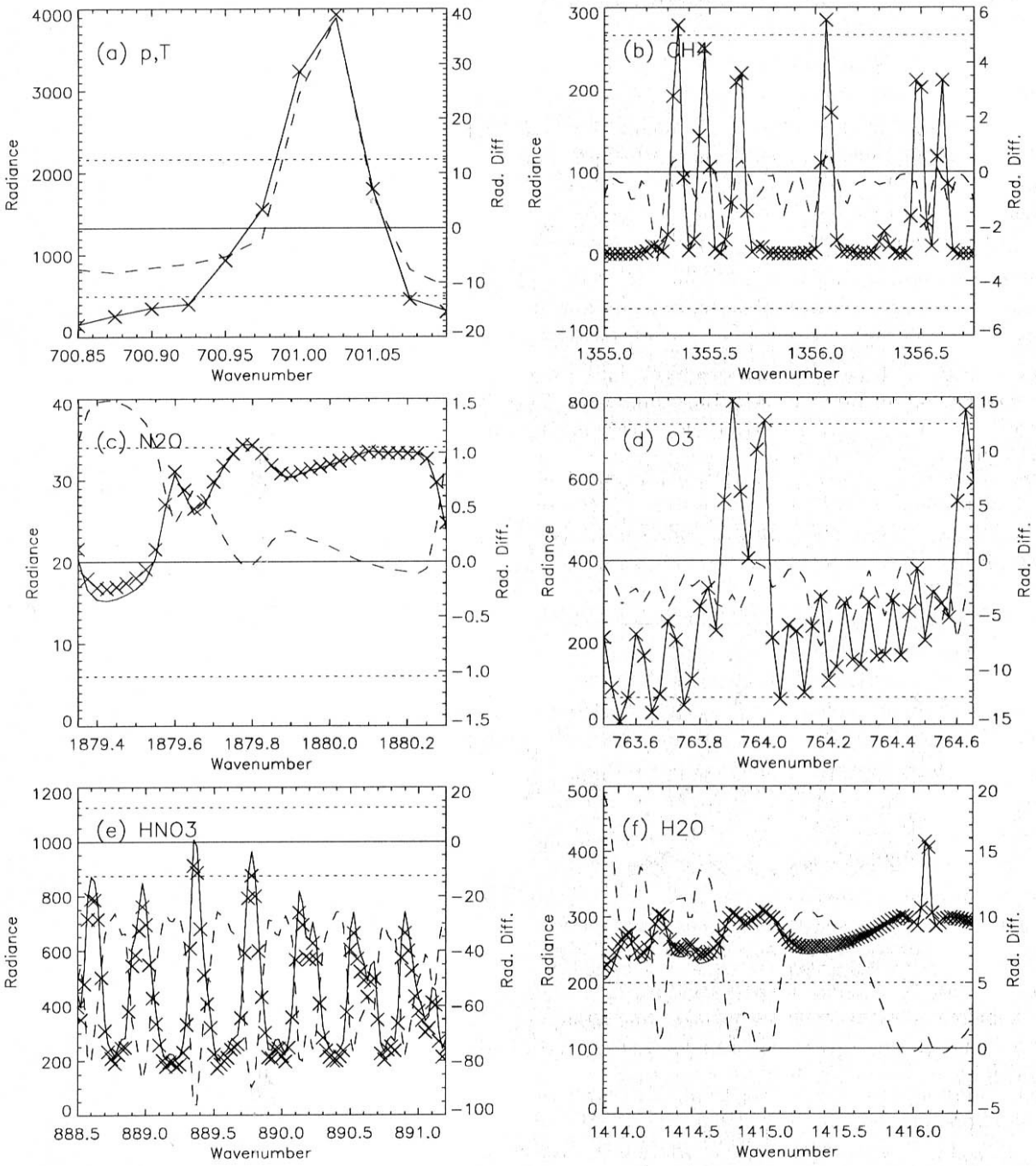

Figure 12: Limb radiance spectra calculated by the current version of the OFM (solid lines) and the original version (crosses). The difference (original−current) is shown by the dashed line.

higher limb views, i.e. the OFM algorithm is more efficient if lines are assigned to particular model altitude ranges rather than to particular tangent altitude ranges. The following approach is adopted:

- If the upper tangent height is $\geq$70 km then the upper model altitude for the line is set to the limit of the atmosphere (100 km)
- If the upper tangent height is <70 km then the upper model altitude for the line is set to upper tangent height + 10 km.

The effect on the vmr microwindows ((b) CH_4, (c) N_2O and (d) O_3) is to increase the radiance to due more stratospheric emission being included, whereas for the p, T microwindow (a) the radiance at line centre is reduced due to mesospheric absorption.

The problem was identified in the p, T microwindow radiance comparison (section 4.3, Fig. 8(a)).

7 Considerations for OFM/ORM Tests

So far the tests have led to a comparison of forward model algorithms for microwindow radiance spectra, making certain modifications to the OFM and RFM to improve the agreement. These modifications will be incorporated into the OFM, and it is also probable that at least some of the RFM reference spectra will regenerated to incorporate the RFM modifications (i.e. those mostly low-altitude spectra that are affected). The following sections describe further results which have a bearing on the outcome of the OFM/ORM retrieval tests.

7.1 Residual Field of View Differences

The FOV convolution, as highlighted previously, remains the outstanding problem in the OFM-RFM intercomparisons, particularly at low altitudes where the water vapour gradient in the upper troposphere is included. To verify this, Fig. 13 shows the same limb radiance calculations in Fig. 11 but without any FOV convolution. This represents the limit of OFM-RFM agreement excluding the FOV differences.

In this case all the 10 km tangent height microwindow differences are now well within NESR/4 (this level of agreement also suggests that there are no significant lines missing from the MIPAS microwindow databases used here).

Two problems can be identified with the present OFM treatment of the FOV:

1. The present scheme does not seem to model adequately the tropospheric gradients, as shown by the H_2O microwindow radiance (Fig. 11(f)) and also by the CO_2 10 km single-line emission test (Fig. 7(c))
2. The use of a quadratic to model strong interference from H_2O lines in other (non-H_2O) microwindows leads to errors where tropospheric water vapour is included in the FOV.

Regarding the first problem, one solution might be to extend the quartic treatment currently used for H_2O microwindows to CO_2, and increase the order of the polynomial used for the H_2O microwindow calculations. This, however, will have an impact on the processing time.

As to the second problem, it should be noted that only a limited number of MIPAS microwindows have strong interference from water vapour lines [16] (the N_2O microwindow used here is not a high-priority microwindow), so if the use of higher-order polynomials is inadequate, it may be possible to avoid the microwindows with strong H_2O interference altogether.

7.2 Equivalent Retrieval Errors

The comparisons so far have concentrated on the differences in radiance spectra, compared to the NESR/4 criterion, which are the natural quantities for evaluating forward models. However, for the OFM/ORM tests the comparison will be between profiles of p, T and vmr: those retrieved by the OFM/ORM compared to those used as RFM input. A Jacobian Analysis (see Appendix) provides a useful means of mapping the forward model differences into the (global-fit) retrieval differences. Note, however, that this does not assume any 'fitted continuum' term, hence systematic offsets will also contribute to the apparent retrieval error.

The results are shown in Table 7.

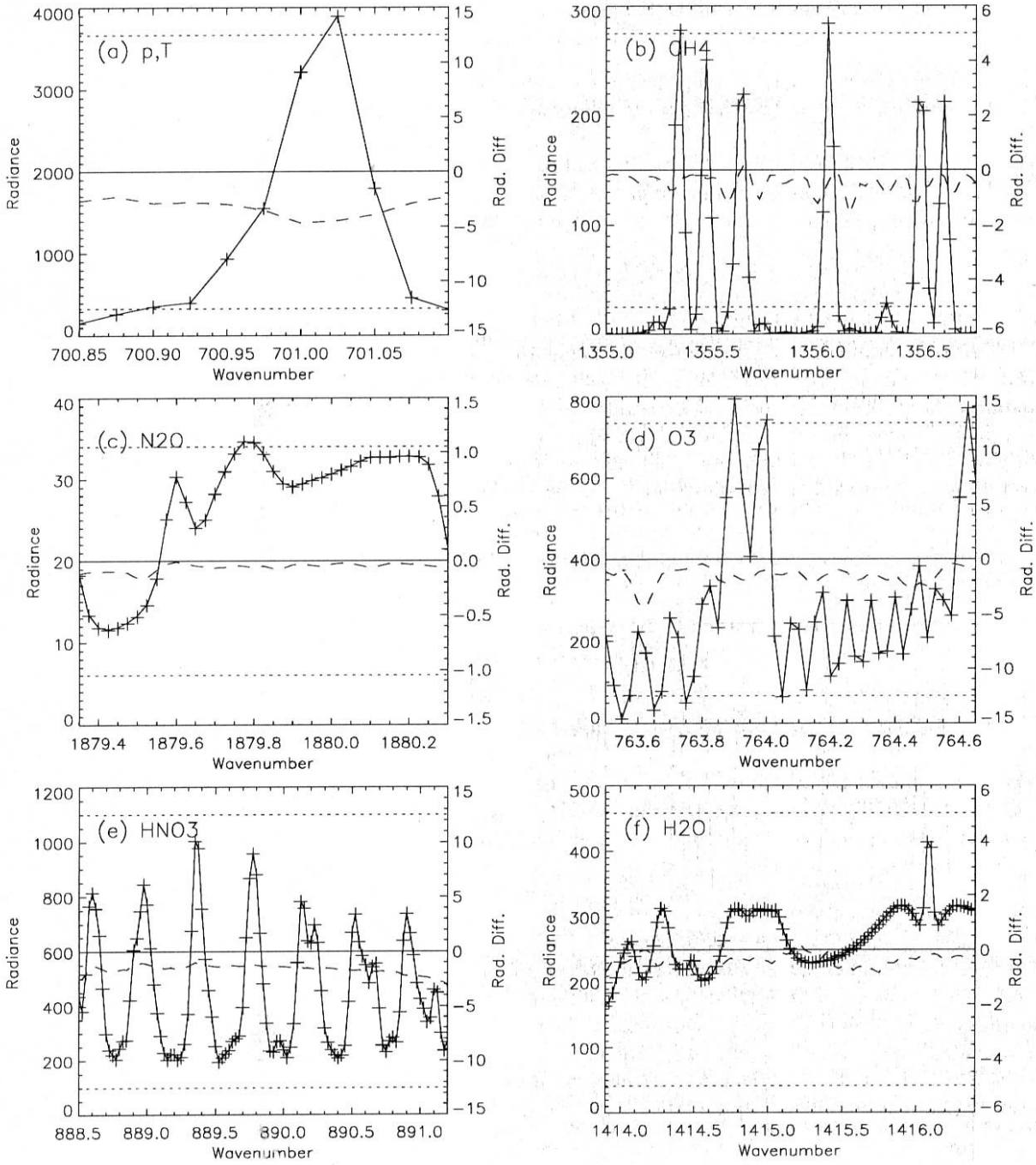

Figure 13: As Fig. 11, except comparing the OFM-RFM without FOV convolution.

Table 7: Equivalent errors in retrieved parameters derived from Jacobian Analyses of radiance difference spectra. The last column shows the acceptance criteria, taken as 25% of the estimated accuracy of the MIPAS retrieval. Temperature errors are in K, others are %.

Parameter	Microwindow	Altitude	RFM v2	RFM Mod.	No FOV	Accept.
Temp.	PT012A	40 km	−0.3	−0.1	−0.1	±0.5
Pres.	PT012A	40 km	−0.6	−0.3	−0.2	±0.75
CH_4	CH440A	40 km	−1.4	−1.5	−0.8	±1.25
N_2O	N2O20A	10 km	−97	−40	−1.7	±1.25
O_3	O3014A	40 km	−0.6	−0.7	−0.7	±1.25
HNO_3	HNO08A	10 km	−0.3	+0.2	−0.4	±1.25
H_2O	H2O17A	10 km	−7.5	−6.7	−0.7	±1.25

The 'RFM v2' column gives the retrieval errors arising from using the RFM v2 radiances (illustrated in Fig. 8), which represents the current state of the RFM v2 (and OFM v2).

The 'RFM Mod' column gives the errors using the modified RFM radiances (illustrated in Fig. 11), which represents the differences if improvements identified in section 5 are implemented in the RFM.

The 'No FOV' column gives the errors expected from the OFM and the modified RFM without any FOV convolution (illustrated in Fig. 13), which might also be the errors expected from the OFM and modified RFM if the FOV-convolution problem is fully resolved.

For the listed microwindows and altitudes, the current forward model discrepancies lie within the acceptance criteria for Temperature, Pressure, O_3 and HNO_3 retrievals (defined as contributing less than 25% of the nominal total retrieval error). The forward model contributions to the N_2O and H_2O retrieval errors are significantly larger than this criterion. In both cases significant improvements should be obtained by accurate FOV-modelling, which brings the H_2O retrieval error within the acceptance criterion, but in the case of N_2O still leaves a residual contribution of 1.7% error. However, it should be reiterated that N2O20A is not a high-priority microwindow for N_2O retrievals.

These results also show that, while the RFM modifications make a significant difference to reducing the radiance discrepancies, the contribution to reducing the retrieval errors are less apparent.

8 Conclusions and Recommendations

The conclusions from each section of tests are as follows:

1. Critical Sub-Modules
   (a) There are no significant discrepancies in the gravity, hydrostatic integration or refractivity algorithms.
   (b) The truncation of the ALS spectral function at ±0.175 cm^{-1} is expected to lead to oscillations of 0.3% of peak value compared with a Fourier-Transformed interferogram.
2. Ray Tracing
   (a) The ray-tracing tests showed no significant discrepancies in the path integrals and Curtis-Godson parameters.
3. Spectral Calculations
   (a) The spectral calculations for homogeneous paths showed 1% differences due to different implementations of the H_2O Continuum, but these are explainable and not considered significant for the retrieval.
   (b) The '96 TIPS model for HNO_3 is inadequate for retrieval purposes and, until better data is available it is recommended that '92 TIPS be used for HNO_3 instead.

4. Limb Spectral Calculations

   (a) The microwindow database shows no evidence of missing 'significant' lines when considering limb radiance calculations within the designated microwindow tangent altitude range.

   (b) The RFM v2 radiative transfer algorithm is inadequate for paths (generally low altitudes) where there are two or more significant absorbers and an approach more consistent with the LTE algorithm is required.

   (c) The RFM 9-pt FOV representation is inadequate for the tropopause region but a 12-pt representation seems to give a significantly improved trade-off between computation speed and accuracy.

   (d) The OFM FOV representation also has problems at 10 km, primarily due to H_2O lines at the tropopause.

The following course of action are recommended:

1. Recompute the low-altitude RFM reference spectra using improved FOV and radiative transfer algorithms.

2. Further investigation of the OFM FOV-convolution algorithm.

3. Repeat tests of the ALS convolution once the operational FFT procedure has been defined.

A Appendix: Jacobian Analysis

The retrieval $\mathbf{x}$ is related to the measurements $\mathbf{y}$ by a contribution function matrix $\mathbf{D}$

$$\mathbf{x} = \mathbf{D}\mathbf{y} \tag{24}$$

Here, y_i are the set of radiances from each spectral element i within a microwindow. The rows $\mathbf{d}_i$ of $\mathbf{D}$ determine the mapping of each spectral element into the solution. Consequently, errors in the forward model ϵ_i will also be mapped into a solution error $\mathbf{e}$ via the same functions.

Consider the simple case where $\mathbf{x}$ is just a scalar x (e.g., tangent point vmr). In this case, the contribution function for each spectral element i is a scalar d_i:

$$x = \sum d_i y_i \tag{25}$$

The problem is to determine d_i.

The global fit approach seeks to find the value x which minimises

$$\sum (y_i - f_i(x))^2 \tag{26}$$

where $f_i(x)$ is the forward modelled-radiance for solution x. Setting the differential of this wrt x as zero gives

$$0 = \sum k_i y_i - k_i^2 x \tag{27}$$

where k_i is the sensitivity (Jacobian, or weighting function) for y_i and it has been assumed that $y_i = k_i x$ (y_i, x may be regarded as small deviations from some linearisation point $\bar{y}_i, \bar{x}$ to ensure this linear relationship applies). Hence,

$$x = \frac{\sum k_i y_i}{\sum k_i^2} \tag{28}$$

Comparing this with Eq. 25 gives the required contribution function:

$$d_i = \frac{k_i}{\sum k_i^2} \tag{29}$$

Strictly, the Jacobian ought to be calculated by just perturbing a single element of the state vector (profile), which requires the forward model input profile to be on the same grid as the retrieval profile. However, it is more convenient to perturb the whole profile on the assumption that the retrieval is sensitive to only that part of the profile near the tangent point.

References

[1] *Development of an optimised algorithm for routine p,T and vmr retrievals from MIPAS limb emission spectra*, Statement of Work PO-SW-ESA-GS-00315, ESTEC, Noordwijk, Netherlands (1995).

[2] Edwards, D. P., *GENLN2: A general line-by-line atmospheric transmittance and radiance model (v3.0)*, NCAR Tech. Note TN-367 + STR, Natl. Cent. for Atmos. Res., 1992.

[3] *Development of a Reference Forward Algorithm for the Simulation of MIPAS Atmospheric Limb Emission Spectra*, Statement of Work PO-SW-ESA-GS-00323, ESTEC, Noordwijk, Netherlands (1995).

[4] Norton, R.H. and R. Beer, New apodizing functions for Fourier spectrometry, *J. Opt. Soc. Am.*, **66**(3) 259–264 (1976) and errata *J. Opt. Soc. Am.*, **67** (3) 419 (1977).

[5] Rodgers, C.D., R.J. Wells, R.G. Grainger and F.W. Taylor, Improved stratospheric and mesospheric sounder validation: General approach and in-flight radiometric calibration, *J. Geophys. Res.*, **101**, 9775–9793 (1996).

[6] *High level algorithm definition and physical and mathematical optimisations*, Tech. Note TN-IROE-RSA9601, IROE, Firenze, Italy.

[7] Allen, C.W., *Astrophysical Quantities*, 3rd Edition. Athlone Press (1973).

[8] Edlén, K., The refractive index of air. *Metrologia*, **2**, 71 (1966).

[9] Kaye, G.W.C., and T.H. Laby, *Tables of Physical and Chemical Constants*, 14th Edition. Longman (1973).

[10] Gallery, G.O., F.X. Kneizys and S.A. Clough, *Air Mass Computer Program for Atmospheric Transmittance/Radiance Calculation: FSCATM*, Air Force Geophysics Laboratory Report AFGL-TR-83-0065, AFGL, Hanscom AFB, Mass., USA (1983).

[11] Humlicek, J., Optimised computation of the Voigt line shape and complex probability functions, *J. Quant. Spectrosc. Radiat. Transfer*, **27**, 437–444 (1982).

[12] Dudhia, A., D.P. Edwards, P.E. Morris and L. Sparks, *Results of Intercomparisons with the RFM Code and External Reference Models.* Tech. Note. PO-TN-OXF-GS-0006, AOPP, Oxford (1996).

[13] Clough, S.A., F.X. Kneizys and R.W. Davis, Line shape and the water vapor continuum, *Atmos. Res.*, **23**, 229–241 (1989).

[14] Edwards, D.P., *MIPAS-RFM High Level Algorithm Definition Document* Tech. Note. PO-TN-OXF-GS-0004, AOPP, Oxford (1996).

[15] Burch, D.E., D.A. Gryvnak, R.R. Patty and C.E. Bartky, Shapes of Collision-Broadened CO_2 lines. *J. Opt. Soc. Am.*, **59**, 267 (1969).

[16] Echle, G., H. Oelhaf, T.v. Clarmann, and M. Schmidt, *Definition of spectral intervals for the retrieval of trace gas concentrations from MIPAS limb emission spectra*, Final Report, ESTEC Contract No.10993/94/NL/PR (1995).